nature astronomy

Article

https://doi.org/10.1038/s41550-026-02816-7

A nearly pristine star from the Large Magellanic Cloud

Received: 24 September 2025

Accepted: 18 February 2026

Published online: 03 April 2026

Check for updates

Alexander P. Ji[1,2,3] ✉, Vedant Chandra[4], Selenna Mejias-Torres[1], Zhongyuan Zhang[1], Philipp Eitner[5,6], Kevin C. Schlaufman[7], Hillary Diane Andales[1], Ha Do[1], Natalie M. Orrantia[1], Rithika Tudmilla[1], Pierre N. Thibodeaux[1], Keivan G. Stassun[8], Madeline Howell[9], Jamie Tayar[10], Maria Bergemann[5], Andrew R. Casey[11,12], Jennifer A. Johnson[9], Joleen K. Carlberg[13], William Cerny[14], José G. Fernández-Trincado[15,16], Keith Hawkins[17], Juna A. Kollmeier[18], Chervin F. P. Laporte[19,20,21,22], Guilherme Limberg[1,2], Tadafumi Matsuno[6], Szabolcs Mészáros[23,24,25], Sean Morrison[26], David L. Nidever[27], Guy S. Stringfellow[28], Donald P. Schneider[29,30] & Riley Thai[11]

The first stars formed out of pristine gas, causing them to be so massive that none are expected to have survived until today. If their direct descendants were sufficiently low-mass stars, such stars could exist today and would be recognizable by having the lowest metallicities (abundance of elements heavier than helium). Here we present the independent identification and detailed chemical analysis of the star SDSS J0715−7334, finding ultralow elemental abundances of both iron and carbon ([Fe/H] = −4.3, [C/Fe] < −0.2) and total metallicity $Z < 7.8 \times 10^{-7}$ ($\log Z/Z_{\odot} < -4.3$). The star's orbit indicates that it originates from the halo of the Large Magellanic Cloud. Its heavy element abundance pattern can be explained by a primordial supernova with an initial mass of 30 solar masses. This star is over ten times more chemically pristine than the most extreme high-redshift galaxies currently found by the James Webb Space Telescope. It is sufficiently metal-poor that current models of low-mass star formation require dust cooling to explain its existence.

The first metal-free (population III) stars are thought to be unusually massive and thus all died in the early Universe[1,2]. Their supernovae synthesized the first metals, fundamentally changing the subsequent thermal evolution of gas and promoting gas fragmentation[3,4]. Thus, the direct descendants of the first stars could have been sufficiently low mass ($\lesssim 0.8\ M_{\odot}$) to survive to the present day and be found in the Milky Way galaxy[5]. The lowest-metallicity star previously known is J1029+1729 (ref. 6), a star in the thick disk of the Milky Way with metallicity $Z < 1.66 \times 10^{-6}$ ($\log Z/Z_{\odot} < -4.0$)[7]. While other stars with lower iron abundances have been found[8–10], they have high carbon abundances and thus higher total metallicities ($\log Z/Z_{\odot} > -3$). A few candidates have been suggested to be as metal-poor as J1029+1729[11,12], but without sufficiently stringent carbon abundance constraints to be certain.

SDSS J0715−7334 was identified in the fifth-generation Sloan Digital Sky Survey (SDSS-V)[13] Milky Way Mapper Halo survey using a `MINESweeper`[14] analysis of low-resolution Baryon Oscillation Spectroscopic Survey (BOSS) spectra[15]. High-resolution follow-up was conducted using the Magellan Inamori Kyocera Echelle (MIKE) spectrograph on Magellan[16] (Fig. 1). Figure 1c shows that no carbon G band is detected, an extraordinary finding for a cool red giant star (effective temperature $T_{\rm eff} = 4{,}700 \pm 100$ K, surface gravity $\log g = 1.1 \pm 0.25$, $[{\rm Fe/H}]_{\rm NLTE} = -4.3$; see Methods for details). We conducted a chemical abundance analysis in one dimension assuming local thermodynamic equilibrium (LTE) and adopting photometric stellar parameters, then corrected the abundances of most elements for non-LTE (NLTE) effects[17]. We paid special attention to the carbon upper limit, using three-dimensional

A full list of affiliations appears at the end of the paper. ✉e-mail: alexji@uchicago.edu

https://doi.org/10.1038/s41550-026-02816-7

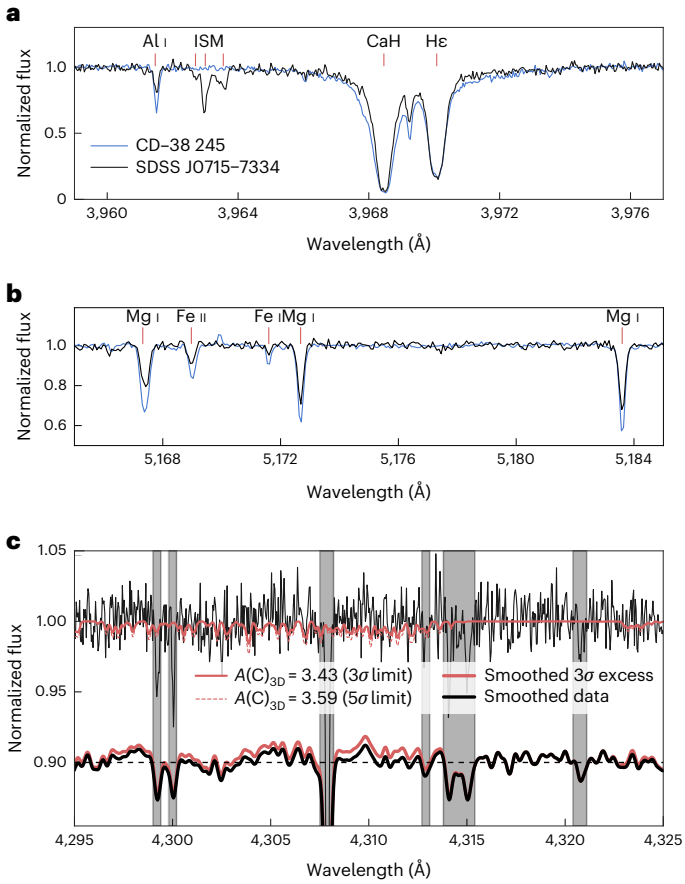

Fig. 1 | J0715−7334 MIKE spectrum. a, CaH and Hε compared with CD−38 245 (blue line) that has $T_{\rm eff}$ = 4,889 K and [Fe/H] = −3.9 [162,182]. J0715−7334 (black line) is narrower in both, indicating that it is both cooler and more metal-poor. Interstellar medium (ISM) lines are also marked. **b**, Mg b region compared with CD−38 245. **c**, CH G-band region. Normal solid and thin dashed red lines indicate synthetic 3D LTE spectra corresponding to a 3σ and 5σ upper limits, respectively. Grey regions are masked as the 3D model includes only CH lines. The thick solid lines offset at +0.9 indicate the smoothed residuals for the 3σ upper limit (red) and the smoothed data assuming no carbon (black). The statistical significance of the upper limit is calculated using a profile likelihood and is related to the integrated area between these two lines (Methods and Extended Data Fig. 1).

(3D) LTE models of the CH molecule[18] and obtaining a 3σ upper limit $A(\mathrm{C})_{\rm 3D} < 3.43$. In addition, stellar interiors convert carbon into nitrogen, which is brought to the surface as stars ascend the red giant branch; correcting for this effect with evolutionary models[19] results in a final $A(\mathrm{C}) < 3.99$ or [C/H] < −4.52 (Extended Data Fig. 1). The adopted chemical abundances including NLTE, 3D and evolutionary corrections are presented in Table 1. The lithium abundance is low, but this is due to depletion on the red giant branch rather than an indication of primordial lithium[20]. This same star was also identified in ref. 12 using Gaia spectra. Their one-dimensional (1D) LTE abundance analysis of a lower-quality spectrum is consistent with our analysis, but without a stringent carbon (and thus total metallicity) constraint (Methods).

Figure 2 shows the iron and carbon abundance of J0715−7334 compared with 38 literature stars with $[\mathrm{Fe/H}]_{\rm LTE} \lesssim -4$ that have detailed chemical abundance measurements. Approximate total metallicity contours are shown as dashed blue lines (Methods). We highlight eight of the stars with the lowest total metallicities as coloured points[6,10,21–26]. We find that J0715−7334 has the lowest metallicity upper limit known, with $Z < 7.8 \times 10^{-7}$, or $\log Z/Z_\odot < -4.3$ using $Z_\odot = 0.016$ (ref. 27) after including NLTE, 3D and evolutionary effects. This is about two times more metal-poor than the metallicity upper limit claimed in the literature for the previous record holder, J1029+1729[7] ($Z < 1.66 \times 10^{-6}$). Our recalculation of this star's metallicity using 3D NLTE results[28] along with the highest signal-to-noise-ratio 3D LTE carbon upper limit[7] gives it a lower metallicity limit ($Z < 9.5 \times 10^{-7}$; Methods). J0715−7334 is over ten times more metal-poor than the most iron-poor star known SMSS J0313−6708 ([Fe/H] < −7.0, [C/H] = −2.55)[29], emphasizing that iron does not track total metallicity at low [Fe/H]. The exact metallicity of J0715−7334 depends on assumptions for unmeasured elements, which dominates the uncertainty. The most important missing elements are nitrogen and oxygen, where we have unconstraining limits from the NH band (Extended Data Fig. 2) and forbidden 6,300 Å oxygen line. The numbers above assume that the missing elements are solar-scaled with [X/Fe] = 0, but other assumptions result in metallicities ranging from (6.7–21.9) × 10^{-7} (or $-4.38 < \log Z/Z_\odot < -3.86$; Methods). In almost all cases, J0715−7334 still has the lowest metallicity upper limit if other stars' metallicities are recomputed using the same assumptions. Similarly, J0715−7334 remains the star with the most metal-poor upper limit known if 1D LTE abundances are assumed for all stars ($Z_{\rm 1D,LTE} < 5.0 \times 10^{-7}$).

We measure a radial velocity from MIKE of +427.2 ± 0.9 km s^{-1} and infer a spectrophotometric distance of $26.1^{+1.5}_{-1.6}$ kpc (Methods). J0715−7334 initially appeared to be unbound from the Milky Way (dashed red line in the top panel of Fig. 3), but its angular momentum and energy is similar to that of the Magellanic Clouds, suggesting a possible association (Methods and Extended Data Fig. 3). We thus integrated the orbit of J0715−7334 in a combined time-evolving potential including the Milky Way and Large Magellanic Cloud (LMC; Methods). A typical orbit is shown in Fig. 3, which follows the LMC as it falls into the Milky Way. This realization has a long-period high-eccentricity orbit around the LMC, but more circular and shorter-period orbits around the LMC are also allowed given the observational uncertainties. Some past orbital realizations are not bound to the LMC, but in this case they are unbound to the Milky Way as well, so we do not consider them to be plausible solutions (Methods and Extended Data Fig. 4). J0715−7334 is thus a galactic immigrant, born in or near the LMC and recently captured by the Milky Way. This contrasts with J1029+1729, which has a Milky Way-thick disk orbit[7,30] and was thus likely born in the Milky Way itself. The other known star in the LMC with $[\mathrm{Fe/H}]_{\rm LTE} < -4$, LMC-119[26], is much more tightly bound to the LMC (Fig. 3, solid yellow line). LMC-119 is also not carbon enhanced, in contrast to the dominant population in the Milky Way halo[5,8,9] and the lowest-mass ultrafaint dwarf galaxies[31,32], suggesting that carbon enhancement may be environment dependent[26].

It is a long-standing question what physics causes the transition from metal-free star formation with a top-heavy initial mass function to the present-day initial mass function[1,2,5]. One idea is that metals change the thermal evolution of gas, causing fragmentation primarily either through carbon and oxygen fine structure line cooling or dust thermal cooling[3,4,33]. The minimum 'critical metallicity' to allow low-mass star formation is $\log Z/Z_\odot \gtrsim -3.5$ for atomic fine structure cooling[3,34] or $\log Z/Z_\odot \gtrsim -5$ for dust thermal cooling[4,33,35,36]. The critical threshold to activate fine structure cooling is often written as $D_{\rm trans} = \log_{10}(10^{[\mathrm{C/H}]} + 0.3 \times 10^{[\mathrm{O/H}]}) > -3.5$ (ref. 34). Previously, J1029+1729 was the only star known with $D_{\rm trans} < -3.5$ (refs. 6,7). Reference 12 suggested that J0715−7334 could also be below the $D_{\rm trans}$ threshold, but its carbon upper limit was too high to be certain. Our stringent carbon upper limit now gives $D_{\rm trans} < -4.2^{+0.3}_{-0.2}$, where the dominant uncertainty is the assumed C/O ratio −1 < [C/O] < 0. Thus, J0715−7334 is now the second known star that can not form through atomic fine structure cooling (Fig. 2), proving that dust cooling is required and also operates in environments beyond the Milky Way. We estimate that >1% of metals must be depleted into dust to explain the formation of J0715−7334, possibly requiring dust grain growth during its protostellar phase (Methods).

The detailed chemical abundances of the most metal-poor stars can be linked back to the properties of metal-free population III stars through supernova nucleosynthesis models[1,2,5]. J0715−7334

https://doi.org/10.1038/s41550-026-02816-7

Table 1 | Chemical abundances of J0715−7334

Element	*N*	*A*(X)	*A*(X)	*A*(X)	[X/H]	[X/Fe]	Δ*A*(X)	σ	σ
		Solar	LTE	NLTE	NLTE	NLTE		[X/H]	[X/Fe]
Li I	1	3.30	<0.33	<0.33	<−2.97	<1.33			
C–H	1	8.51	<3.88	<3.99	<−4.52	<−0.22	+0.11		
N–H	1	7.94	<4.56	<4.56	<−3.38	<0.92			
O I	1	8.76	<6.91	<6.91	<−1.85	<2.45			
Na I	2	6.30	1.86	1.92	−4.38	−0.07	+0.06	0.12	0.09
Mg I	6	7.57	3.23	3.49	−4.08	0.22	+0.26	0.12	0.11
Al I	2	6.46	1.12	1.43	−5.03	−0.73	+0.31	0.13	0.09
Si I	1	7.55	3.04	3.28	−4.27	0.03	+0.24	0.18	0.13
K I	1	5.12	<2.18	<2.18	<−2.94	<1.37			
Ca I	2	6.33	1.87	2.08	−4.25	0.06	+0.21	0.13	0.10
Ca II	2	6.33	2.05	2.07	−4.26	0.04	+0.02	0.24	0.17
Sc II	3	3.08	−1.43	−1.43	−4.51	−0.21		0.21	0.13
Ti II	13	4.94	0.29	0.62	−4.33	−0.02	+0.33	0.14	0.07
Cr I	2	5.67	0.57	0.60	−5.08	−0.77	+0.03	0.16	0.11
Mn I	1	5.52	−0.12	0.56	−4.96	−0.65	+0.68	0.30	0.27
Fe I	58	7.49	2.97	3.19	−4.30	0.00	+0.22	0.13	
Fe II	6	7.49	2.76	2.76	−4.73	−0.42	−0.00	0.15	
Co I	2	4.91	0.51	1.39	−3.52	0.79	+0.88	0.20	0.14
Ni I	6	6.25	1.28	1.28	−4.97	−0.66	−0.00	0.16	0.08
Zn I	1	4.65	<1.49	<1.49	<−3.16	<1.15			
Sr II	1	2.93	<−3.35	<−3.35	<−6.28	<−1.97			
Ba II	1	2.22	<−3.31	<−3.31	<−5.53	<−1.22			

N is the number of lines used. The *A*(X) NLTE, [X/H] and [X/Fe] columns are provided in 1D NLTE when possible, using the correction in the Δ*A*(X) column. The correction for C–H is not using NLTE, but instead calculated as the difference between the 1D LTE analysis and the combination of a 3D correction of −0.45 dex (ref. 18) and an evolutionary correction of +0.56 dex (ref. 19). Solar abundances adopted are from refs. 27,199. [X/Fe] is computed using [Fe I/H]. Abundance uncertainties on [X/H] and [X/Fe] differ because they consistently propagate correlations with respect to stellar parameters.

is an especially clean probe of population III, as its distant halo orbit completely precludes significant surface contamination from the interstellar medium[37,38] and its large convective envelope removes any diffusive settling effects. Figure 4 shows the result of a fit to the detailed elemental composition of J0715−7334 using theoretical metal-free supernova yields[39] (Methods). Stringent upper limits are placed on the neutron-capture elements (Extended Data Fig. 5) but not used in the fit. Overall, this star is best explained by a 30 $M_{\odot}$ progenitor star and a high explosion energy around 5×10^{51} erg. A weighted average and standard deviation gives $M_{\rm prog} = 27.0 \pm 3.9\ M_{\odot}$ and $E_{\rm expl} = 6.0 \pm 2.6 \times 10^{51}$ erg (Methods). Leave-one-element-out tests show that the initial mass fit is driven by the C upper limit (ruling out models around 10–15 $M_{\odot}$) and Na and Mg (shifting the best-fit mass up from 25 $M_{\odot}$ to 30 $M_{\odot}$). Elements affecting the explosion energy are Ca and Mn (ruling out the 10^{52} erg models) and Co (preferring models $>3 \times 10^{51}$ erg).

As the two most metal-poor stars known, it is worth comparing the population III progenitors for J0715−7334 with J1029+1729. J1029+1729 has a population III progenitor with low initial mass 10–20 $M_{\odot}$ (ref. 28) and a low explosion energy $\lesssim 1.5 \times 10^{51}$ erg, while J0715−7334 has a population III progenitor with much higher initial mass 25–35 $M_{\odot}$ and a high explosion energy $\gtrsim 5 \times 10^{51}$ erg. These two stars originate in clearly different environments. We speculate that this could be an early indication of environment dependence in population III star formation, a scenario known as population III.2[40,41]. The LMC forms several comoving megaparsecs away from the proto-Milky Way[26], close enough for radiative feedback but not chemical feedback[42]. Thus, its population III star formation could be affected by Lyman Werner or ionizing radiation from the proto-Milky Way, which in turn may change the population III initial

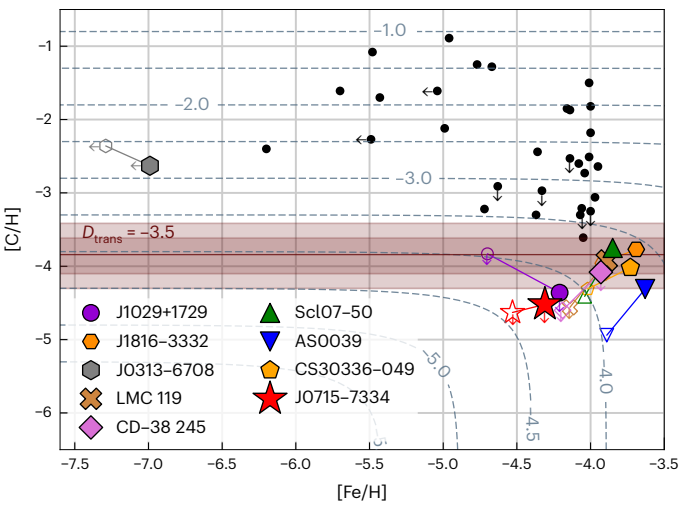

Fig. 2 | Carbon and iron abundances of ultra-metal-poor stars. J0715−7334 is shown as a large red star. Black points show a literature sample[30,176]. Coloured points highlight eight other notable stars, with 1D LTE abundances shown as small open symbols and a combination of 1D NLTE, 3D LTE and 3D NLTE analyses shown as large solid coloured symbols (Methods). The dashed blue contours indicate an approximate total metallicity assuming [Mg/Fe] = +0.4 (Methods). A horizontal dark red line indicates the critical $D_{\rm trans}$ threshold[3,34] for atomic fine structure line cooling assuming [C/O] = −0.6 (ref. 189), and the two shaded regions show −1 < [C/O] < 0 and an extra 0.2 dex theoretical uncertainty[3].

https://doi.org/10.1038/s41550-026-02816-7

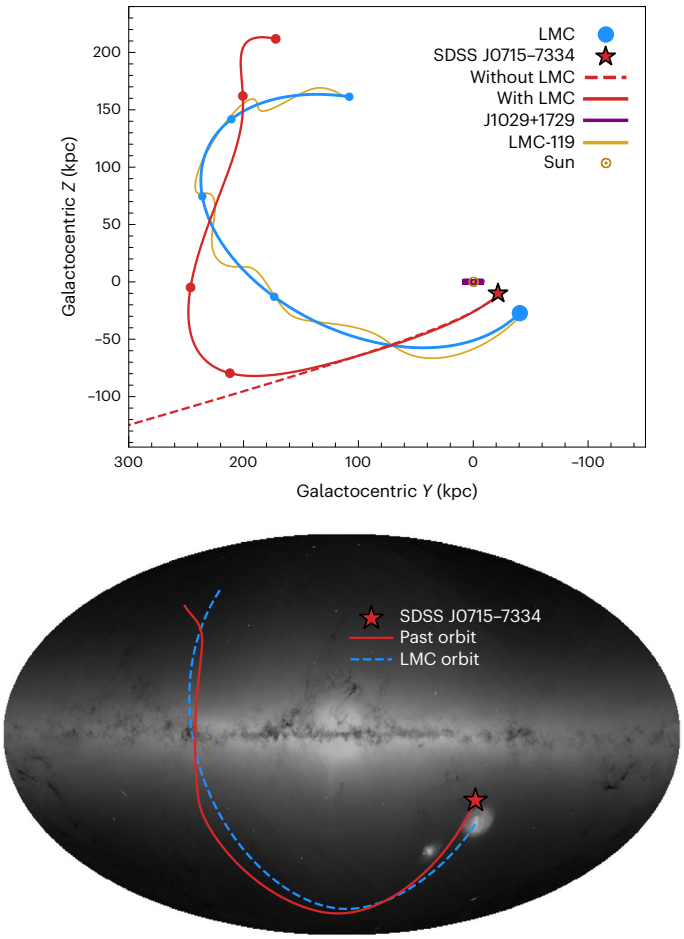

Fig. 3 | Kinematic properties. Top: past orbit of J0715−7334 over 4 Gyr in Galactocentric coordinates, integrated in a potential that includes the gravitational influence of the LMC (solid lines). Circular markers are placed every 1 Gyr. For comparison, the past orbit of the LMC itself is shown, along with orbits of the stars J1029+1729 (confined to the disk) and LMC-119 (closely bound to the LMC). The dashed red line shows the unbound orbit of J0715−7334 in a Milky Way-only potential. Bottom: the past orbit of J0715−7334 and the LMC in Galactic coordinates on-sky, overlaid on the distribution of all stars observed by Gaia. Credit: background ESA/Gaia image, A. Moitinho, A. F. Silva, M. Barros, C. Barata, University of Lisbon; H. Savietto, Fork Research, under a Creative Commons license CC BY-SA 3.0 IGO.

mass function[1,2,43]. However, many more similarly metal-poor stars will need to be found in different environments to test this hypothesis.

The launch of the James Webb Space Telescope has led to a flurry of discoveries of extremely metal-poor high-redshift galaxies[44–46]. The metallicity upper limits have been claimed to be as low as [Z/H] < −3. These are undoubtedly exciting objects, but the metallicity constraints remain an order of magnitude away from legitimate claims of detecting population III stars. The lowest [O III]/Hβ ratio measured so far is <0.22 (ref. 46), but a galaxy with the same metallicity as J0715−7334 would have [O III]/Hβ < 0.01 (ref. 47). Thus, at least ten times better signal-to-noise ratios are needed to show that these high-redshift galaxies are not population II galaxies composed of stars like J0715−7334. The search for population III stars continues.

Methods

Observations

The SDSS-V[13] has been executing an all-sky survey of the Milky Way halo since 2021, using twin BOSS spectrographs[48] at the Apache Point Observatory and Las Campanas Observatory. These halo stars are targeted using a variety of spectrophotometric selections that prioritize distant and metal-poor stars[15]. SDSS J0715−7334 was observed by BOSS at the Las Campanas Observatory on 16 December 2024 for a single 15-minute exposure, which achieved signal-to-noise ratios of about 25 per pixel. The coordinates of the star are $(\alpha, \delta) = (108.91087°, -73.58141°)$, the Gaia source ID is Gaia Data Release 3 (DR3) 5262850721755411072, the Two Micron All-Sky Survey (2MASS) ID is 2MASS J07153858−7334530, and the SDSS ID is SDSS_ID 95803549. The star was targeted for belonging to the infrared colour-selected metal-poor candidate selection of ref. 49 and a distant red giant selection[15,50–52]. Stellar parameters were determined using the `MINESweeper` pipeline of the SDSS-V halo survey[14,15]. The pipeline estimated a metallicity [Fe/H] ≈ −3.8 for SDSS J0715−7334, near the lowest edge of the allowable parameter grid and the lowest metallicity of stars observed in SDSS-V so far. Visual inspection showed the star was clearly near the tip of the red giant branch (RGB), but no metal absorption lines beyond a weak calcium K line were detected in the BOSS spectrum, flagging SDSS J0715−7334 for high-resolution spectroscopic observations.

We obtained 225 minutes of high-resolution follow-up spectroscopy of J0715−7334 on 21–22 March 2025 with the MIKE spectrograph[16] on the Magellan/Clay telescope. We used the 0.7 arcsecond slit, which provides resolution 35,000 in the blue and 28,000 in the red (split at approximately 5,000 Å). The data were reduced with CarPy[53], obtaining signal-to-noise ratios of (50, 85, 165) per pixel at (4,000 Å, 4,500 Å, 6,500 Å), respectively, with about 2 pixels per resolution element. The heliocentric radial velocity was 427.2 ± 0.9 km s^{-1}, where the uncertainty is calculated using the order-to-order scatter that quantifies the dominant wavelength calibration uncertainty[31]. The velocity differs from the SDSS-V measurement by about 2σ, but systematic wavelength calibration uncertainties of about 10 km s^{-1} are known in SDSS-V[15] so this is not evidence for binarity. Spectra were normalized and stitched using the

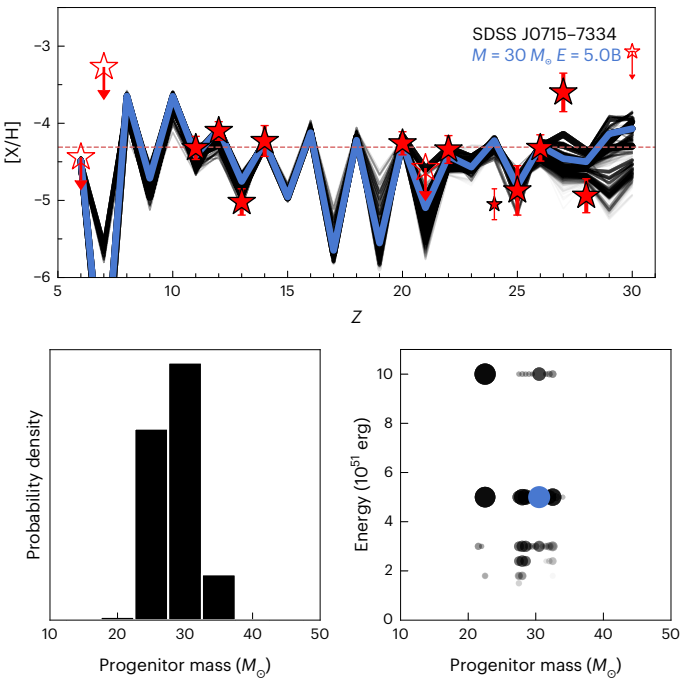

Fig. 4 | Population III supernova progenitor constraints. Top: chemical abundance pattern of J0715−7334. Filled red stars show measured abundances with 1σ uncertainties; open red stars with arrows are upper limits (treated as hard cut-offs). Sc is treated as an upper limit due to model uncertainties; Cr and Zn are excluded[39]. The blue line shows the best-fit model; black lines show other models within 95% confidence, with opacity indicating fit quality. The initial mass (M) and explosion energy in Bethe (E) are shown at the top. Bottom left: progenitor mass distribution of models weighted using total absolute error (Methods). Bottom right: explosion energy versus progenitor mass for the same models; point size scales with fit quality. Best-fit model shown in blue.

LESSPayne environment[54], which combines The Payne[55] with the smhr graphical user interface[56].

Stellar parameter analysis

We adopt an effective temperature $T_{\rm eff}$ = 4,700 ± 100 K and surface gravity log g = 1.10 ± 0.25 based on a consideration of photometry, spectroscopy and asteroseismology as detailed in the following section. The resulting metallicity is [Fe/H] = −4.53 ± 0.2, assuming 1D LTE. This star is at the extreme end of essentially all model grids considered, but this range covers what we consider to be all reasonable solutions.

Photometric stellar parameters were determined in 5 ways and obtained $T_{\rm eff}$ = 4,650–4,800 K and log $g \approx$ 1.1. First, we used 6 colour–temperature relations[57] based on Gaia DR3 G, BP and RP photometry; 2MASS K_s photometry; and the ref. 58 extinction of A_V = 0.50 to obtain $T_{\rm eff}$ = 4,668 ± 16 K. Next, we derived colour–temperature and colour–gravity relations from the most metal-poor isochrones available for the MIST, Dartmouth, PARSEC and BaSTI isochrones considering the same 6 colours and extinction, resulting in $T_{\rm eff}$ = 4,678 ± 36 K and log g = 1.06 ± 0.15. Using the larger ref. 59 reddening A_V = 0.58 resulted in $T_{\rm eff}$ = 4,726 ± 38 K and log g = 1.17 ± 0.15. Third, we used the isochrones package[60] with MultiNest[61] and MIST isochrones[62] to fit the zero point-corrected Gaia DR3 parallax[63–68] and photometry from GALEX NUV[69]; SkyMapper DR4 uvgriz[70]; Gaia DR3 G[63,64,67,68,71,72]; 2MASS JHK$_s$[73]; and Wide-field Infrared Survey Explorer CatWISE2020 W1W2W3[74–77]. We adopt a uniform V band extinction prior $0 < A_V < 1$ mag; a distance prior based on a parallax-only geometric distance[78] but increasing the uncertainty by a factor of 5; and a log-uniform age prior from 1 Gyr to 13.8 Gyr. The MIST isochrones do not allow [Fe/H] below −4, so we used a uniform prior −4.0 < [Fe/H] < −3.5. This results in stellar parameters $T_{\rm eff} = 4{,}780^{+20}_{-20}$ K, log $g = 1.04^{+0.06}_{-0.05}$ with reddening $A_V = 0.65^{+0.04}_{-0.03}$, corresponding to a distance $d = 25.6^{+1.3}_{-1.7}$ kpc. Inspection of the results suggested they could potentially be affected by finite sampling of the isochrone near the tip of the red giant branch, so we ran another test using a more finely sampled MIST isochrone fixing [Fe/H] = −4 and using only redder photometry like Gaia RP, 2MASS JHK$_s$ and WISE W1W2, which resulted in essentially the same result of $T_{\rm eff}$ = 4,787 K, log g = 1.1, distance d = 24.3 kpc with A_V = 0.58. Finally, for an independent atmosphere model, we used the PHOENIX stellar atmospheres[79] to fit the broadband spectral energy distribution using 2MASS JHK$_s$; WISE W1W2W3; Gaia G, BP, RP and XP spectrophotometry; and GALEX NUV, resulting in $T_{\rm eff}$ = 4,750 ± 50 K with A_V = 0.625 (refs. 80,81).

Spectroscopic stellar parameters were determined in 3 ways and obtained $T_{\rm eff}$ = 4,500–4,600 K. First, we performed a 1D LTE analysis with an empirical temperature correction[82]. We measured equivalent widths of Fe I and Fe II lines, then used MOOG with scattering[83–85] and ATLAS model atmospheres[86,87] to ensure no trend in Fe line abundances with respect to excitation potential, ionization state and reduced equivalent width. We then applied the empirical temperature correction and rebalanced the Fe lines holding the temperature fixed, resulting in $T_{\rm eff}$ = 4,540 K, log g = 0.95, [Fe/H] = −4.77 and microturbulence ξ_t = 1.62 km s^{-1}. We also used TSFitPy[17], which uses Turbospectrum[88] and the standard MARCS model atmospheres[89] along with precomputed NLTE departure coefficients for Fe (ref. 90) from MULTI[91], and attempted to find a NLTE spectroscopic balance. Our solution reached the edge of the departure coefficient grid at $T_{\rm eff}$ = 4,500 K, but the final solution would need to have a lower temperature. Fixing $T_{\rm eff}$ = 4,500 K, we found log g = 1.4, [Fe/H] = −4.65 and ξ_t = 1.6 km s^{-1} in 1D NLTE. Using a lower temperature would further lower log g and the metallicity. Finally, we ran a fit to the Hβ Balmer line profile. We used Korg[92,93] to generate the hydrogen line profiles, then simultaneously fit the temperature, surface gravity, metallicity and continuum[94]. The results suggested a temperature $T_{\rm eff} \approx$ 4,600 K, with uncertainties driven primarily by how much of the H core was masked. Note that we could not use the Hα Balmer line profile in this star as it shows substantial emission features associated with mass loss at the tip of the red giant branch. There are also small emission features in the Ca HK line cores that may also suggest some level of chromospheric activity in this star.

Finally, we put a constraint on log g with asteroseismology using photometry from the Transiting Exoplanet Survey Satellite (TESS) mission[95]. J0710−7334 is located in the southern continuous viewing zone of TESS, which currently has a total of 2.8 years of observations. We detrended the time-series photometry by ref. 96: downloading TESS photometry from the Mikulski Archive for Space Telescopes (MAST) database using the tesscut Python package[97]; manually defining aperture masks in the TESS full-frame images; using the regression corrector function in LightKurve[98] to remove systematic background trends for each sector separately; stitching light curves together without filling large gaps; and computing the Lomb–Scargle periodogram[99,100] of the full light curve to obtain the power spectrum. To reduce the noise in the final stitched light curve, we omitted sectors with light curves that showed long-term trends in the photometry after the regression corrector step. In total, we used 27 sectors of TESS data, equating to an observational duty cycle of 2 years. Despite the considerable length of the observations, the resulting asteroseismic signal had a low signal-to-noise ratio, and we treat it as a marginal detection. This can be attributed to the star's faint magnitude, which is at the detectability limit of the TESS instrument. Using the asteroseismic pipeline pyMON[101], a tentative measurement for the frequency of the maximum acoustic power was found to be $\nu_{\rm max}$ = 18 μHz. This corresponds to a surface gravity of log $g_{\rm seismic}$ = 2.2 using the seismic scaling relation[102]: $g_{\rm seismic} \propto \nu_{\rm max} T_{\rm eff}^{0.5}$. There are known deviations from the seismic scaling relations for metal-poor stars, where masses larger than expected are estimated[103,104]. To reconcile this, a scaling factor to the $\nu_{\rm max}$ quantity is implemented in the seismic scaling relations, consequently reducing the seismic mass and log $g_{\rm seismic}$ estimates[105,106]. Calibrations of the $\nu_{\rm max}$ scaling factor require detailed modelling of the individual frequency peaks, which is unfeasible for J0715−7334 given the low signal-to-noise ratio of the asteroseismic signal. Therefore, we conclude that lower log g values cannot be ruled out with asteroseismology and thus adopt log $g_{\rm seismic}$ = 2.2 as an upper bound. This still excludes the higher log g spectroscopic solutions, which could be biased due to the small number of Fe II lines available.

It is clear that systematic modelling choices for such an extreme cool and metal-poor star dominate the overall stellar parameter uncertainty. We thus decide to adopt an intermediate value $T_{\rm eff}$ = 4,700 ± 100 K. Putting this temperature range into the MIST, Dartmouth, PARSEC and BaSTI isochrones results in log g = 1.1 ± 0.25. These $T_{\rm eff}$ and log g ranges cover essentially all values in the exploration above. Using these stellar parameters, balancing Fe I abundances with respect to reduced equivalent width in 1D LTE with MOOG and ATLAS results in ξ_t = 1.60 km s^{-1}, and we adopt a 0.3 km s^{-1} systematic uncertainty as many log g–ξ_t relations predict $\xi_t \approx$ 2.0 at such low log g values[107]. We adopt a model metallicity [M/H] = −4.53 ± 0.15, and for our fiducial ATLAS analysis we use [α/Fe] = 0.0, although adopting [α/Fe] = +0.4 results in nearly identical abundances. The stellar parameter uncertainties will dominate the chemical abundance uncertainties.

The final choice of stellar parameters results in a significant ionization imbalance between [Fe I/H] = −4.30 and [Fe II/H] = −4.73, a 2.1σ difference given the quoted uncertainties. This is a common occurrence in the analysis of the most metal-poor red giant stars with [Fe/H] $\lesssim$ −3 (refs. 108–110). One suggested possibility is that the Fe I NLTE corrections are too large at such low [Fe/H][7,110], even though they are clearly more accurate at higher metallicities [Fe/H] $\gtrsim$ −2.5 (ref. 111). We also verified that similar or larger NLTE corrections are consistently found across many independent calculations with different atomic data and model atmospheres[90,112–114]. Another possibility is that our adopted surface gravity from isochrones is too low. This would require the stellar evolution models to be incorrect, which, for example, could occur if the mixing length varies substantially between [Fe/H] = −2.5 where the isochrones have been empirically checked against globular clusters

and [Fe/H] < −4 (refs. 115,116). We investigated several metal-poor red giants with Gaia DR3 parallaxes and compared our purely photometric log g derivation with that using the fundamental Stefan–Boltzmann law, finding offsets within 0.1 dex. In particular, CD−38 245 is a [Fe/H] = −4 red giant with a parallax signal-to-noise ratio >14 in Gaia DR3. We photometrically derive log g = 1.48 ± 0.19, while using geometric distances[78] with colour–temperature relations[57] and bolometric corrections[117] obtains log g = 1.58 ± 0.07. Thus, there is no clear solution to the ionization imbalance, reflecting the current state of the literature.

One option to avoid the question of ionization imbalance would be to adopt the Fe II abundance as the metallicity for this star, as is often done for metal-poor red giants[109,118]. We decided to keep the NLTE-corrected Fe I abundance as our fiducial value as most of the stars in this metallicity range do not have Fe II lines, and this also produces a more conservative upper limit on the metallicity of J0715−7334 ($\log Z/Z_\odot < -4.3$ instead of $\log Z/Z_\odot < -4.7$).

Chemical abundance analysis

We start with a standard 1D LTE chemical abundance analysis on all elements using `LESSPayne`[54] and `TSFitPy`[17]. The 1D LTE `LESSPayne` analysis uses `MOOG` with scattering and interpolates ATLAS model atmospheres from a precomputed grid. A new line list was constructed by identifying all visible absorption lines in the spectrum, then adopting atomic data from `linemake`[119]. This uses laboratory data when possible, and Kurucz atomic data when not possible. Nearly all element abundances were determined using equivalent widths fit using Gaussian profiles in `LESSPayne`. This includes species such as Al I and Si I that would normally require syntheses in iron-poor stars due to large carbon enhancements, and we verified that there were no blends in these lines. However, we synthesized three iron-peak species (Sc II, Mn I, Co I) due to hyperfine structure splitting. In addition, for non-detections of Li I, O I, K I, Zn I, Sr II and Ba II, we determined upper limits by finding the best-fit model of the continuum and abundance simultaneously, then increasing the abundance until $\Delta\chi^2 = 25$, close to a formal 5σ upper limit[118]. C and N constraints are based on molecular bands that require a more careful continuum treatment and discussed later.

To check systematic uncertainties on the model atmosphere, line list and radiative transfer code, we also conducted a 1D LTE abundance analysis using `TSFitPy`[17], which wraps `Turbospectrum`[88] and uses the standard MARCS model atmospheres[89]. The line list was from Gaia-ESO[120] and extended with VALD[121] down to λ > 3,700 Å, so the `TSFitPy` analysis is restricted to redder lines. We iteratively synthesized synthetic spectra in LTE and calculated their equivalent widths, matching them to the measured equivalent widths. Differences between the `MOOG`/ATLAS analysis and the `Turbospectrum`/MARCS analysis are included as a contribution to the per-line systematic uncertainty (`dLTE`).

We then determined detailed line-by-line abundance uncertainties using `LESSPayne`. For each spectral line i, we calculate statistical, stellar parameter and systematic uncertainties. Statistical uncertainties ($e_{\mathrm{stat},i}$) are obtained by propagating equivalent width uncertainties on Gaussian fits from `LESSPayne`, including continuum placement[118]. Stellar parameter uncertainties are calculated by re-determining the abundances in 3 alternative stellar parameter scenarios: cooler (T_{eff} = 4,600 K, log g = 0.85, ξ_t = 1.60, [Fe/H] = −4.64; `dSP1`), warmer (T_{eff} = 4,800 K, log g = 1.35, ξ_t = 1.60, [Fe/H] = −4.41; `dSP2`), and ξ_t uncertainty (T_{eff} = 4,700 K, log g = 1.10, ξ_t = 1.90, [Fe/H] = −4.53; `dSP3`). For each line, we then subtract the abundances obtained with the alternative set of stellar parameters from those obtained with the fiducial set of stellar parameters, for example, $\mathtt{dSP1}_i = \log \varepsilon_{i,\mathrm{cool}} - \log \varepsilon_{i,\mathrm{fuducial}}$. With these abundance differences, we calculate the total stellar parameter uncertainty by taking the quadrature sum $e^2_{\mathrm{SP},i} = max(|\mathrm{dSP1}_i|, |\mathrm{dSP2}_i|)^2 + \mathrm{dSP3}_i^2$. Systematic uncertainties s_i for each line are calculated by taking the largest of three uncertainties: the difference between MOOG/ATLAS and Turbospectrum/MARCS ($\mathtt{dLTE}_i$), a systematic uncertainty such that adding statistical and systematic uncertainties matches the line-to-line standard deviation[118], and a minimum per-line systematic floor of 0.1 dex.

For each chemical species X, we calculate the abundance log ε(X) as an inverse-variance weighted average, $\log \epsilon(\mathrm{X}) = \sum_i w_i \log \epsilon_i / \sum_i w_i$. We adopt per-line weights $w_i = \left[e^2_{\mathrm{stat},i} + e^2_{\mathrm{SP},i} + s_i^2\right]^{-2}$ that include the per-line statistical, stellar parameter and systematic uncertainties. The stellar parameter uncertainties for species X are also calculated using the weights, for example $\mathtt{dSP1}_\mathrm{X} = \sum_i w_i \mathtt{dSP1}_i / \sum_i w_i$. To calculate the total statistical uncertainty, we take $\sigma^{-2}_{\mathrm{stat},X} = \left[\sum_i 1/(e^2_{\mathrm{stat},i} + s_i^2)\right]$, excluding the stellar parameter uncertainty as this is included differently for [X/H] and [X/Fe]. The uncertainty on log ε(X) is then given by $\sigma^2_\mathrm{X} = \sigma^2_{\mathrm{stat,X}} + \max(|\mathrm{dSP1_X}|, |\mathrm{dSP2_X}|)^2 + \mathrm{dSP3}^2_\mathrm{X}$, which is also the uncertainty on [X/H]. The uncertainty on [X/Fe] adds statistical uncertainties for both X and Fe, then accounts for the correlated errors on X and Fe with respect to stellar parameters, that is $\sigma_{\mathrm{[X/Fe]}} = \sigma^2_{\mathrm{stat,X}} + \sigma^2_{\mathrm{stat,Fe}} + \max(|\mathrm{dSP1_X} - \mathrm{dSP1_{Fe}}|, |\mathrm{dSP2_X} - \mathrm{dSP2_{Fe}}|)^2 + (\mathrm{dSP3_X} - \mathrm{dSP3_{Fe}})^2$. In general, the uncertainties on [X/Fe] are lower as the stellar parameter uncertainties partially cancel out.

Finally, we calculated non-LTE corrections for most elements using `TSFitPy`. Departure coefficients are precomputed from model atoms for sodium and aluminium[114], magnesium[111], silicon[122,123], calcium[113,124], titanium[125], chromium[126], manganese[127], iron[90,124], cobalt[128,129] and nickel[130,131]. Only lines from 3,700 Å to 9,200 Å are used. We calculate line-by-line NLTE corrections, given by the column $\mathtt{dNLTE}_i$, then do the same weighted sum as above to determine a total NLTE correction for each species. The total corrections are shown in Table 1. We adopt the 1D NLTE abundances as our final abundances.

Carbon and nitrogen upper limits

Special care was taken when deriving abundances or upper limits using molecular bands, namely, the CH G band for carbon and the NH band at 3,360 Å for nitrogen. This is because for weak molecular bands, there is a well-known degeneracy between the continuum level and the strength of the molecular bands[7], requiring careful treatment of normalization. The typical analysis fixes the normalization and then places the upper limit by increasing the abundance until $\Delta\chi^2$ surpasses some set threshold[28,118]. Owing to concerns about normalization accuracy, often only the strongest individual features are used[7], but this neglects weaker features that should strengthen the upper limit.

Here we use the profile likelihood[132,133] to determine CH and NH upper limits that account for continuum normalization uncertainties. Given a model spectrum with abundance A(X) and nuisance continuum parameters $\mathcal{C}$, one can use a χ^2 distribution model with one degree of freedom to describe the likelihood of A(X), while accounting for $\mathcal{C}$ (ref. 134). In other words, we compute a grid of synthetic spectra at different values of A(X), optimizing $\mathcal{C}$ at each value of A(X) and using the resulting χ^2 contour to determine detections and upper limits. For the purpose of determining upper limits, this is significantly more conservative than the standard approach: as A(X) increases, the best-fit continuum level also increases, resulting in a higher A(X) than if the continuum were previously fixed.

The carbon upper limit for J0715−7334 was determined using 3D LTE models of the CH G band. The model atmosphere for this star was computed using the 3D radiation-hydrodynamics code `M3DIS`[18,135]. We set the physical extent of the simulation domain to 10^{10} m in the horizontal direction and 5×10^9 m in the vertical direction. We then evolve the atmosphere with a grid resolution of 260 × 260 × 130 points for ~25,000 h ≈ 2.9 yr of stellar time to ensure that the final model is sufficiently relaxed. Owing to the wide range of physical scales involved, it is very difficult and time-consuming to evolve 3D atmospheres of metal-poor giants towards a specific T_{eff}, as it is an output quantity in 3D rather than an input. Because the complexity further increases with increasing pressure scale height ($\sim T/g$) we chose to adopt a model that converged to $T_{\mathrm{eff}} \approx$ 4,660 K with log g = 1.25 and [Fe/H] = −4.5 for

the 3D analysis, and later apply a correction for the difference. The post-processing synthesis of the G band was done using an updated version of the MULTI3D[18,136] code and uses the Masseron[137] CH line list. The CH strength depends on the oxygen abundance due to the C/O ratio, and we adopt a scaled-solar oxygen value in the analysis. We synthesized G-band spectra for A(C) ranging from 2.06 to 4.31 in increments of 0.25 dex. Each synthetic spectrum was created by averaging the results from ten snapshots of the same simulation, which were chosen to span at least one convective turnover time to properly account for the dynamic nature of the 3D atmosphere.

With the 3D model grid in place, the carbon upper limit was determined with the profile likelihood. The signal-to-noise ratio in the G-band region is 70 per pixel or 100 per resolution element. We fixed the spectral smoothing to 0.14 Å full-width at half-maximum based on nearby detected lines and mask all absorption lines that are not due to carbon features. The CH G band covers two different echelle orders on MIKE. Rather than normalize and stitch the two orders, we modelled the continuum of each order separately to avoid any spectral interpolation that would affect the noise properties. For each order, we adopt a seventh-degree polynomial, which was selected by running our upper-limit procedure for polynomial degrees between 3 and 13 and picking the lowest-order model that minimized the Akaike information criterion[138]. The choice is purposefully conservative: lower polynomial degrees result in more stringent carbon upper limits by 0.1–0.2 dex, as they do not allow a slight continuum increase right above the carbon bands. Higher polynomial degrees >11 are sufficiently flexible to introduce an artificial 1–2σ detection by raising the continuum only above the CH bands while still matching the continuum outside of those regions. We then adopted a 3σ (99.9% confidence) upper limit, corresponding to $\Delta\chi^2 = 10.273$ for one degree of freedom. We also calculate a 5σ upper limit corresponding to $\Delta\chi^2 = 26.338$.

The results are shown in Extended Data Fig. 1, giving a 3σ upper limit A(C) < 3.23. The left panels show the actual data being fit, that is, two spectral orders with the same spectral model but different continua and non-carbon regions being masked. The top-middle panel shows a stitched version of the left panels, assuming the continuum fit from a model with almost no carbon. The dashed red line indicates the profile likelihood continuum for the 3σ limit, which differs from the minimum χ^2 continuum because it is re-fit for each A(C) value. The bottom-middle panel shows the error-normalized residual, where the statistical significance comes from integrating the difference between the red and blue curves. The right panel shows the difference in χ^2 as a function of A(C), determining a 3D upper limit of A(C) < 3.23, or −0.65 dex lower than our nominal 1D LTE abundance upper limit of A(C) = 3.88. To estimate the impact of using different stellar parameters, we also calculated the upper limits in 1D LTE at our fiducial $T_{\rm eff}$ = 4,700 K and log g = 1.10 and the 3D atmosphere values $T_{\rm eff}$ = 4,660 K and log g = 1.25. The upper limit differs by 0.20 dex, so we shift the 3D LTE abundance by the same value, resulting in A(C) < 3.43. This is −0.45 dex lower than the 1D LTE upper limit. We checked that an inaccurate wavelength calibration would result in <0.02 dex increase to the carbon upper limit.

It is worth noting that 1D atmospheres do not account for the adiabatic cooling that is present in 3D atmospheres and is responsible for decreasing the temperature in the outer layers of the model atmosphere[139] and strengthening the carbon abundance limit[7,18]. We thus also use a set of lower-resolution models to estimate the differences in three dimensions. We find that the changing temperature results in $\lesssim$0.1 dex differences and changing log g results in ~0.2 dex differences, leading to a +0.3 dex correction instead of the +0.2 dex correction adopted above. Increasing the carbon abundance by 0.1–0.2 dex increases the total metallicity by 0.1 dex and would not change the conclusions of this paper.

During the first dredge up and after the red giant branch bump, mixing with the stellar interior brings up the products of the CNO cycle and increases the surface nitrogen abundance while decreasing the carbon abundance[140]. Thus, the observed carbon abundance is lower than the natal carbon abundance, the observed nitrogen abundance is higher than the natal nitrogen abundance, and the total number of carbon and nitrogen atoms is conserved. Stellar evolution models can be used to estimate the amount of carbon correction, and we use a precomputed correction grid from ref. 19. We find an evolutionary correction of +0.56 dex. As the physics of extra mixing and the carbon correction is somewhat uncertain and the star's log g is near the red giant branch bump at this metallicity[141,142], we ran MESA models of the red giant branch as an independent check on the evolutionary correction, which obtained essentially identical results to the precomputed grid. In summary, the total correction to the 1D LTE carbon abundance is −0.45 + 0.56 = +0.11 dex. Thus, our final adopted carbon abundance limit is A(C) < 3.99 or [C/H] < −4.52, including both 3D and evolutionary effects.

The nitrogen constraint in such metal-poor stars comes from a very blue NH band at 3,360 Å. Extended Data Fig. 2 shows this region of the spectrum, which is very noisy (signal-to-noise ratios of 3 per pixel, 4 per resolution element) as our star is a faint and cool red giant. The smoothed version of the spectrum shows a possible NH detection visible at the strongest region at 3,360 Å. We again apply the profile likelihood to estimate the value of a detection or upper limit in 1D LTE with MOOG/ATLAS. Working in the range 3,350–3,370 Å, we use a second-order polynomial to model the continuum, again chosen to minimize the Akaike information criterion. The right panel of Extended Data Fig. 2 shows the resulting χ^2 profile. The minimum χ^2 is achieved at $A(\mathrm{N}) = 4.10^{+0.18}_{-0.25}$. Unlike the case of CH, here we can visually detect a feature in the smoothed spectrum, and the polynomial order is also very low, leaving a possibility that this is a detection. However, we conservatively adopt a 3σ (99.9% confidence) upper limit of A(N) < 4.56 as the current nitrogen constraint. We expect the limit would decrease substantially in a 3D analysis similar to carbon. In addition, the natal N abundance was lower depending on the number of C atoms that were converted to N during the main sequence lifetime. If we assume a detection at the A(C) upper limit, the carbon correction of +0.56 dex corresponds to a decrease in A(N) of −0.09 dex. We do not apply this downwards correction to N, as it would be a smaller correction if the carbon abundance is below the upper limit.

Kinematic analysis and Magellanic association

The kinematic parameters of SDSS J0715−7334 are estimated using the adopted spectrophotometric distance of $d_{\rm helio}$ = 26.1 kpc and radial velocity $v_{\rm r}$ = 427.2 km s^{-1}. All kinematic calculations are performed on 10^4 Monte Carlo realizations of the star's present-day phase-space position, with the median and half-difference between the 16th and 84th quantiles being adopted as the parameters with 1σ uncertainties. For the Gaia DR3 proper motions, we utilize the full covariance information when generating these realizations. A right-handed Galactocentric frame is assumed with a solar position $\mathbf{x}_\odot$ = (−8.12, 0.00, 0.02) kpc, and solar velocity $\mathbf{v}_\odot$ = (12.9, 245.6, 7.8) km s^{-1} (refs. 143–145).

Extended Data Fig. 3 shows the kinematics of J0715−7334 as a large red star, other ultra-metal-poor stars, and the LMC and the Small Magellanic Cloud (SMC) as coloured points, and a shaded grey background of the entire SDSS-V halo sample[15]. The top panel of Extended Data Fig. 3 shows the energy (assuming the static MilkyWayPotential2022 potential from gala[146]) and L_Z angular momentum component. Notably, J0715−7334 has total energy >0, naively suggesting that it is unbound from the Milky Way. However, this ignores the influence of the Magellanic Clouds. The LMC (and SMC) are notable for their high orbital velocity, which manifests as a large angular momentum in the Galactocentric reference frame, particularly along the L_X coordinate. This extreme angular momentum signature is a powerful tool to search for stars that originate in the Magellanic Clouds[52]. Thus the bottom panel of Extended Data Fig. 3 shows the space of Galactocentric angular momentum in the L_Z–L_X space. J0715−7334 has angular

momenta similar to the LMC and SMC, and falls securely in the region of angular momenta occupied by Magellanic Debris. J0715−7334 has a negligible angular momentum in the unseen dimension, with $L_Y \approx 0.9$ km s^{-1} kpc. Therefore, SDSS J0715−7334 has an orbital trajectory similar to the Magellanic Clouds.

To further investigate the past orbit of J0715−7334, we integrate back its phase-space position in a time-varying potential that includes the gravitational influence of the LMC[52,147]. This calculation is implemented in `agama`[148]. Specifically, we adopt the `MilkyWayPotential2022` from `gala`[146], which has a circular velocity at the solar position $v_c(R_\odot) = 229$ km s^{-1} (ref. 149). The LMC is modelled as a rigid $1.8 \times 10^{11}\,M_\odot$ Navarro, Frenk and White (NFW) profile that matches current observational constraints[150]. The LMC is integrated back from its current position taking into account dynamical friction, which defines the time-varying potential[151–153]. The orbit of J0715−7334 is subsequently integrated in this time-varying potential, again for 10^4 Monte Carlo realizations of the present-day phase-space position. A typical (median) orbit is shown in Fig. 3, which also shows the ultra-metal-poor stars J1029+1729 and LMC-119 integrated in the same potential for comparison. J1029 +1729 remains confined to the Milky Way disk, whereas LMC-119 is firmly bound to the LMC as expected.

A random subset of orbits is shown in Extended Data Fig. 4, colour-coded by the future fate of J0715−7334. About 60% of orbits have a pericentre with respect to the LMC of 5–50 kpc, and apocentres within the LMC virial radius (~120 kpc). In other words, they clearly originate from the LMC. Indeed, compared with the Magellanic Stellar Stream members from ref. 52, SDSS J0715−7334 has one of the most confident kinematic associations with the LMC. However going forward, these orbits do not remain bound to the LMC. They are highly eccentric orbits with apocenters with respect to the Milky Way ranging from 150 kpc to 250 kpc, while the LMC continues to sink deeply into the Milky Way potential due to dynamical friction. Thus, these solutions (shown in blue in Extended Data Fig. 4) correspond to J0715−7334 being an LMC halo star that comes in with the LMC system and subsequently remains bound to the Milky Way.

The other 40% of orbits are not previously bound to the LMC, that is, they do not have a close pericentre with the LMC in the last 4 Gyr. However, these same orbits are completely unbound and will leave the combined Milky Way–LMC system in the future (orange lines). These solutions correspond to stars originating from the cosmic web with such high peculiar velocities that they pass straight through the Milky Way, but coincidentally they line up with the Magellanic Clouds' current orbital configuration. Such solutions are highly implausible compared with the case that J0715−7334 originates from the LMC system.

The detailed orbit within the LMC has substantial uncertainties (Extended Data Fig. 4). About half the orbits have more eccentric orbits and tighter pericentres <20 kpc, while the other half have more circular orbits and larger pericentres. There are additional modelling uncertainties, such as the LMC's mass and halo shape, the amount of dynamical friction, and the interaction with the SMC. These uncertainties should not alter the association of J0715−7334 with the LMC, but would affect whether J0715−7334 is best interpreted an in situ LMC halo star or part of the LMC's accreted halo.

Comparison with Limberg et al.

Recently, Limberg et al.[12] made an independent identification of the same star using Gaia XP spectra[154]. Their follow-up spectra also used Magellan/MIKE, but only 40 minutes of data compared with our 225 minutes. They obtained stellar parameters $T_{\rm eff} = 4{,}596 \pm 65$ K, $\log g = 0.88 \pm 0.15$ cgs, $\xi_t = 2.27 \pm 0.10$ km s^{-1} and [Fe/H] = −4.82 ± 0.25 from a 1D LTE analysis. The metallicity is 0.3 dex lower than our 1D LTE analysis. Their photometrically determined temperature is 100 K smaller than our fiducial value, which is at the coolest end of what we infer, and they adopted the Yonsei–Yale isochrones[155,156] to determine $\log g$, which accounts for that difference. Due to the lower signal-to-noise ratio of that spectrum, they adopt an empirical $\log g$–ξ_t relation[107] that results in a much higher ξ_t, but this higher ξ_t is inconsistent with our measured Fe I line strengths. If we restrict only to the strongest, relatively saturated lines measured in our spectrum and adopt their stellar parameters, we can reproduce their conclusions. About half of the 0.3 dex difference in [Fe/H] is attributed to their lower temperature and the other half to their higher microturbulence. Due to the low signal-to-noise ratio of the spectrum, they could only put a relatively high upper limit [C/Fe] < +0.5 ([C/Fe]$_{\rm corr}$ < +1.2 after evolutionary corrections) and measured element abundances from fewer lines resulting in abundances consistent with ours within the uncertainties.

The higher signal-to-noise ratios, improved upper limit analysis, and additional NLTE and 3D analyses in this work are necessary for a stringent total metallicity constraint and comparison with theoretical yield models that were not possible by Limberg et al. In particular, we can put a $D_{\rm trans}$ constraint that is clearly below the critical threshold. They derived [C/H] < −3.64, which results in $D_{\rm trans} = -3.5 \pm 0.1$, right at the threshold $D_{\rm trans} = -3.5 \pm 0.2$. We derive $D_{\rm trans} = -4.2^{+0.3}_{-0.2}$, clearly below the threshold. We are also able to perform a meaningful comparison with supernova yields with the more accurate NLTE chemical abundances and better abundance precision.

In principle, our results could be improved by combining both datasets. We tested combining their data with ours and rerunning the analysis, finding a negligible change in results. To illustrate, we focus on the CH upper limit that is most sensitive to improved signal-to-noise ratios. In the G-band region, the median signal-to-noise of the coadded spectrum would have increase from 70 per pixel to 75 per pixel and naively result in a better upper limit. However, we find no change to the upper limit when including the new data. This is because we optimize over uncertainties in continuum placement for each new order instead of rebinning and coadding the data (to avoid introducing pixel correlations that affect the χ^2 analysis), and the uncertainties in continuum placement remove the benefit of the higher total signal-to-noise ratio. We thus use only our higher-quality spectrum in our analysis.

Limberg et al. also perform a kinematic analysis. The radial velocity and proper motion data are identical to ours, and in particular there is no radial velocity variation between the two MIKE observations. They adopt a slightly larger distance due to their lower $\log g$ value. Although Limberg et al. also find evidence for an association with the LMC, with over 50% of their orbit calculations having a long-term pericentre below 60 kpc (ref. 52), we here have also shown that the orbits not bound to the LMC are unbound from the Milky Way (Extended Data Fig. 4). We thus claim a much stronger likelihood of association with the LMC than Limberg et al.

Literature data sample

We identified 38 stars[5,6,10,11,21–26,157–175] with $[{\rm Fe/H}]_{\rm 1D,LTE} \lesssim -4$ in the literature, shown in Figs. 2 and 3. The stars were primarily identified in the JINABase literature compilation[176] and supplemented using the SAGA literature compilation[177] and other recent references. We excluded stars that had only low-resolution spectroscopy and thus only Fe and C abundances, although many such stars are known[178,179].

We put a special focus on eight stars owing to their extremely low total metallicities, extreme abundances and/or orbits: the previous record holder for the most metal-poor star J1029+1729[6,7,28,180], the first nearly ultra-metal-poor star in the inner galaxy J1816−3332[23], the most iron-poor star known J0313−6708[10,29], the previous LMC metal-poor record holder LMC-119[26], the first most metal-poor star known CD−38 245[21,181,182], two ultra-metal-poor stars in the Sculptor dSph Scl07-50[24] and AS0039[25,183], and an ultra-metal-poor halo star CS30336-049[22]. The stars J1029+1729[28] and J0313−6708[29] have full 3D NLTE analyses where possible, and 3D LTE for CH and NH. The stars AS0039[25] and CD−38 245[182] have full 1D NLTE analyses. For the other four stars, we determined 1D NLTE corrections to the Fe abundances[90] and carbon evolutionary corrections[19] to place them on Fig. 2. A star of note that

is not included is Pristine_221[11], which has the potential to be similarly metal-poor with $[Fe/H]_{LTE} = -4.8$. However, this star has a very loose carbon upper limit [C/H] < −2.5 (ref. 184), so it may still have a high overall metallicity.

The detailed chemical abundances of the whole sample in 1D LTE are shown in Extended Data Fig. 5, highlighting J0715−7334, J1029+1729 and SMSS J0313−6708. We use 1D LTE here as NLTE and 3D analyses are not available for the vast majority of stars, but we apply evolutionary corrections to carbon[19]. The background sample is shown as a boxplot for each element. J0715−7334 has one of the lowest carbon abundances of any star known, which along with its very low iron abundance is what makes it the most metal-poor star currently known. It also has the second-lowest Sr and Ba abundances known. SMSS J0313−6708 has lower abundances of almost every element including the lowest Fe abundance known, but it has such high C (and O (ref. 185)) abundances that its total metallicity is quite high $\log Z/Z_\odot = -2.7$. J1029+1729 is a relatively faint and ultra-metal-poor dwarf star, so fewer elements are available but enough have been measured to determine a strong metallicity upper limit and abundance pattern[7,28,180]. Especially notable is that it has a very low Na and Mg abundance, which has been attributed to either an explosion of a relatively low-mass star (10–20 $M_\odot$)[28] or surface pollution from the interstellar medium[7]. We emphasize that not all core-collapse supernovae must produce high [Mg/Fe] ratios; the Mg production correlates strongly with a star's initial mass and can be low for the lowest-mass core-collapse supernovae[186].

We also computed kinematics for all 38 stars consistently with J0715−7334. Radial velocities were obtained from the literature references. Distances were derived using photometry and parallax from the `isochrones` package, with the same extinction, metallicity and distance priors as before. For the three stars known to be in Sculptor and the LMC, we use the distance of the host galaxy as a prior. One star (SDSS J174259.67+253135.8) has insufficient information for a good distance so is not included in the kinematic compilation. Overall, we draw the same qualitative conclusions as the kinematic study in ref. 30, including that a vast majority of stars with low $|z_{max}|$ are prograde, and that J1029+1729 is on a thick disk orbit consistent with forming in the proto-Milky Way or in an extremely early accretion event[187].

Total metallicity calculation

The total metallicity Z of a star is given by[28]:

$$Z = \frac{1 - Y}{1 + X/Z}$$

where we assume a primordial helium mass fraction $Y = 0.2477$ (ref. 188) and the metals-to-hydrogen mass ratio is

$$\frac{Z}{X} = \sum_i \left[10^{A(i)-12}\mu(i)\right]$$

where $A(i)$ is the abundance of element i and $\mu(i)$ is the atomic weight of element i.

As not all elements are measured in stars, one must extrapolate the missing elements to determine the metallicity. In the main text, we report a metallicity calculated the simplest way (method 1), which is to assume each missing element scales with overall iron abundance such that [X/Fe] = 0 for all elements X, that is, fill them in with solar ratios. We adopt the recent ref. 27 solar abundance pattern for the solar ratios, which has total metallicity $Z_\odot = 0.016$. This provides $Z < 7.85 \times 10^{-7}$ or $\log Z/Z_\odot < -4.31$. A possibly more accurate way is to correlate the missing elements with another element that more closely traces the nucleosynthetic pathways that produce a particular element, for example, [X/Mg] = 0 for elements correlated with Mg. As a first estimate, we associate C, N and O with the carbon abundance (light elements); F to Ca with the Mg abundance (alpha-elements); and Sc and up with the Fe abundance (Fe peak and neutron-capture elements). This assumption (method 2, motivated by ref. 7) leads to a slightly lower value $Z < 7.61 \times 10^{-7}$ or $\log Z/Z_\odot < -4.32$. To estimate metallicities for many stars, if only C, Mg and Fe are measured, one can derive an equation for the total metallicity:

$$Z = 31.22 \times 10^{A(\mathrm{C})-12} + 118.93 \times 10^{A(\mathrm{Mg})-12} + 45.69 \times 10^{A(\mathrm{Fe})-12}$$

This equation, assuming [Mg/Fe] = +0.4, is used to calculate the blue contours in Fig. 2.

As the most abundant metal that is almost always unmeasured, the assumption for the oxygen scaling is the most important systematic effect. If instead oxygen scales as an alpha-element with Mg instead of C (method 3), we obtain $Z < 10.5 \times 10^{-7}$ or $\log Z/Z_\odot < -4.18$. If we hold all missing elements at solar composition then fix [O/Fe] = +0.6 (method 4, following ref. 28), this gives $Z < 18.0 \times 10^{-7}$ or $\log Z/Z_\odot < -3.95$. Finally if we adopt [C/O] = −0.6 similar to most other metal-poor stars[189], this gives $Z < 21.9 \times 10^{-7}$ or $\log Z/Z_\odot < -3.86$ (method 5). Under almost all of these assumptions, J0715−7334 remains the most metal-poor star known, with J1029+1729 being the second-most metal-poor star. We calculate that for methods 1–5, J1029+1729 has metallicities $\log Z/Z_\odot < -4.23, -4.29, -4.34, -3.86$ and -3.61, respectively. Note that we derive a lower-metallicity upper limit for J1029+1729 than ref. 7 when using the same assumptions (method 2) because we also adjust N and O when applying the 3D correction to carbon, while they change only C. Under these varying assumptions, J1029+1729 has a total metallicity upper limit consistently 0.05–0.25-dex-more metal-rich than the metallicity upper limit of J0715−7334. The exception is if O scales with Mg, due to the higher Mg abundance in J0715−7334. Redoing the calculations assuming a solar pattern with lower oxygen abundance[190] gives 0.06-dex-lower total metallicities throughout. Either way, these two stars clearly stand out from other known stars as having $\log Z/Z_\odot < -4$ under all assumptions, thus robustly requiring that they form under the influence of dust cooling[33].

There are currently some discrepancies in the literature on the chemical abundances of J1029+1729. Here we adopt the 3D NLTE abundances (or 3D LTE when not available) from ref. 28 for all elements except C, where we adopt the 3D LTE abundances from the recent analysis in ref. 7. This choice is made as we consider the 3D NLTE analysis to include the maximum amount of relevant physics for analysing metal-poor stars, but ref. 7 analysed a spectrum with about 4 times more data, which should produce the strongest upper limit on C. Focusing on the 3D and/or NLTE abundances of key elements, Lagae et al. find $A(\mathrm{C}) < 4.86$, $A(\mathrm{Mg}) = 3.18$ and $A(\mathrm{Fe}) = 3.28$. Reference 7 found $A(\mathrm{C}) < 4.11$, $A(\mathrm{Mg}) = 3.00$ and $A(\mathrm{Fe}) = 2.91$. If we adopt all of the ref. 7 abundances, we find the two stars J0715−7334 and J1029+1729 have very similar total metallicities primarily due to a much smaller NLTE correction to Fe, and which star is more metal-poor depends entirely on the assumption of the abundance of missing elements. This is evident if we calculate a lower limit on the total metallicity by setting all unmeasured elements to 0 abundance: both J0715−7334 and J1029+1729 have $Z > 1.84 \times 10^{-7}$ or $\log Z/Z_\odot < -4.94$. If the ref. 7 abundances are more accurate, then much deeper observations that constrain more elements in both stars, especially oxygen, will be needed to discern which star has a more metal-poor upper limit. We note that it is unlikely in the near future to obtain such constraints on J1029+1729 as there are no detections in 29 hours of Ultraviolet and Visual Echelle Spectrograph (UVES) data, but as a cool and fairly bright red giant there is a chance that OH and NH could be detected in J0715−7334.

Population III yield fits

We use the metal-free core-collapse supernova yield models in ref. 39 to fit the chemical abundance pattern of J0715−7334. Due to uncertainties in the underlying yield models, we follow the recommendation to ignore our Cr measurement and Zn upper limit, and we treat the model

prediction for Sc as a lower limit (that is, our measured Sc is an upper limit), which is indicated by different size points shown in Fig. 4. We did include the non-constraining upper limits on O and K in the fit, but these are not plotted in Fig. 4 for clarity. The best-fit models are found by minimizing the error-normalized total absolute error (TAE)[191]:

$$\mathrm{TAE} = \sum_{\mathrm{X}} \left| \frac{[\mathrm{X/H}]_{\mathrm{obs}} - [\mathrm{X/H}]_{\mathrm{model}}}{\sigma_{\mathrm{X}}} \right|$$

We use the TAE instead of χ^2 because we expect the fits to be dominated by systematic uncertainties, and the TAE penalizes outliers less than χ^2. This is then an optimization over four parameters: the progenitor mass M, the final kinetic explosion energy E, the mixing parameter ξ, and the dilution factor D. In practice, we find the best-fit D for all 16,800 models through a brute-force search initialized at the analytic minimum χ^2 solution. We reject all models that are inconsistent with our upper limits, then take the best-fit result as the model with the smallest TAE.

We adopt a weight for each of the 16,800 models assuming that the data are distributed according to a Laplace distribution, which is appropriate for minimizing the TAE. The per-species uncertainty σ_{X} is turned into a Laplace scale $b_{\mathrm{X}} = \sigma_{\mathrm{X}}/\sqrt{2}$. Assuming that the likelihoods satisfy Wilks' theorem[134], we calculate twice the negative log likelihood and assign a weight $w \propto \exp[-\sqrt{2}\ \mathrm{TAE}]$. We use these weights to estimate the best-fit progenitor mass and explosion energy for J0715−7334 as a weighted sum and standard deviation, finding $M = 27.0 \pm 3.9\ M_{\odot}$ and $E = (6.0 \pm 2.6) \times 10^{51}$ erg, although the energy uncertainty is strongly affected by discreteness effects. We also use these weights to construct the weighted histogram in the bottom left panel of Fig. 4 and determine the opacity and size of lines and points in the other two panels. As each plotted line has the same opacity, the thick black regions in Fig. 4 indicate areas where many models overlap.

Critical metallicity calculations

The critical metallicity for atomic fine structure cooling is driven primarily by the carbon and oxygen line cooling[3]. It can be described as[34]:

$$D_{\mathrm{trans}} = \log_{10}\left(10^{[C/H]} + 0.3 \times 10^{[O/H]}\right) > -3.5 \pm 0.2$$

which is similar to $\log Z/Z_{\odot} > -3.5$. This threshold assumes that nearby Lyman Werner radiation is sufficient to dissociate all molecular hydrogen in the collapsing gas cloud, which could otherwise somewhat lower the critical metallicity threshold by providing some additional cooling[192].

As none of the most metal-poor stars have oxygen measurements, computing the D_{trans} criterion requires an assumption for the [O/H] abundance. In this metal-poor regime, it is physically most appropriate to choose [O/H] based on the [C/O] ratio (instead of for example an [O/Fe] ratio), because C and O have tighter correlations both observationally[177,189] and theoretically from core-collapse supernova nucleosynthesis calculations[39,191]. For Fig. 2, the horizontal dark red line indicates the conversion from $D_{\mathrm{trans}} = -3.5$ to a critical [C/H] = −3.84 by adopting the typical value [C/O] = −0.6 from the [C/O] plateau in metal-poor stars[189]. The narrow shaded uncertainty region ranges from $-4.10 < [\mathrm{C/H}] < -3.61$, corresponding to a fairly extreme range of values $-1 < [\mathrm{C/O}] < 0$ that spans most data and nucleosynthesis models[39,177]. Higher [C/O] ratios are possible (for example, the carbon-enhanced metal-poor stars) but would not affect the total metallicity. The widest uncertainty region adds ±0.2 dex on top of this range, due to theoretical uncertainties in the temperature and density of gas assumed to calculate D_{crit} (ref. 3). Even in the extreme case [C/O] = −1 and $D_{\mathrm{trans}} = -3.7$, J0715−7334 is clearly below the fine structure cooling threshold. It is only the second star to be below this threshold, along with J1029+1729[7].

The critical metallicity for dust thermal cooling is driven primarily by silicate grains (for example, enstatite $MgSiO_3$ and forsterite Mg_2SiO_4) or amorphous carbon grains[33,36,193–195]. Amorphous carbon is not important for J0715−7334 due to its low carbon abundance[36]. It is possible to calculate a critical abundance threshold for dust cooling, although it depends on the grain species being considered, the grain size distribution that can be characterized by characteristic size $a_{\mathrm{cool}} = \langle a^3 \rangle / \langle a^2 \rangle$, and the dust depletion factor $0 \leq f_{\mathrm{dep}} \leq 1$ (refs. 33,36,194).

Reference [36] provides an estimate for the critical Mg abundance assuming silicates can be characterized by enstatite, whose production is limited by the key element Mg:

$$[\mathrm{Mg/H}]_{\mathrm{cr}} = -4.70 + \log\left(\frac{a_{\mathrm{cool}}/f_{\mathrm{dep,MgSiO_3,Mg}}}{0.1\,\mu\mathrm{m}}\right)$$

Given an [Mg/H] measurement, we can put a lower limit on the depletion factor of Mg by rearranging:

$$f_{\mathrm{dep,MgSiO_3,Mg}} > 10^{-[\mathrm{Mg/H}]-4.70}\left(\frac{a_{\mathrm{cool}}}{0.1\,\mu\mathrm{m}}\right)$$

For J0715−7334 with [Mg/H] = −4.07 and assuming a typical grain size of 0.01–0.1 μm (refs. 33,196), this gives $f_{\mathrm{dep,MgSiO_3,Mg}} \gtrsim 0.02 - 0.2$. Doing the same calculation for forsterite (key element Si) gives

$$f_{\mathrm{dep,Mg_2SiO_4,Si}} > 10^{-[\mathrm{Si/H}]-4.75}\left(\frac{a_{\mathrm{cool}}}{0.1\,\mu\mathrm{m}}\right)$$

or for J0715−7334 with [Si/H] = −4.27 gives $f_{\mathrm{dep,Mg_2SiO_4,Si}} \gtrsim 0.03 - 0.3$. We conservatively estimate that the minimum depletion factor of these elements is 1%. This potentially places constraints on the physics of early dust production: because the explosion energy we infer for the supernova progenitor of J0715−7334 is quite high ($E_{\mathrm{expl}} \gtrsim 5 \times 10^{51}$ erg), we expect that the supernova reverse shock would be especially effective at destroying dust grains[193], leading to low dust depletion that can be well below 1% after a strong shock[33]. However, dust grain growth during protostellar collapse can increase the depletion factor back up to ≳1% (ref. 195). A similar conclusion can be reached using J1029+1729[35,197], and it is somewhat remarkable that, despite the very different formation environments and supernova progenitors (mass, explosion energy), the conclusions about dust properties can be similar.

Data availability

The BOSS spectrum of J0715−7334 (`sdss_id` 95803549) will become publicly available in SDSS Data Release 20, as will the background halo star sample of `MINESweeper` results. The individual line measurements, normalized MIKE spectrum, and literature star abundances and kinematics are available at https://doi.org/10.5281/zenodo.18483957 (ref. 198).

Code availability

Most codes used for analysis are publicly available on GitHub, including `LESSPayne`[54], `MOOG`[83–85], `TSFitPy`[17], `Turbospectrum`[88] and `agama`[148]. The exception is that `M3DIS`[18] and the version of `Multi3D` used are not public yet, but a public release is planned.

References

1. Bromm, V., Yoshida, N., Hernquist, L. & McKee, C. F. The formation of the first stars and galaxies. *Nature* **459**, 49–54 (2009).
2. Klessen, R. S. & Glover, S. C. O. The first stars: formation, properties, and impact. *Annu. Rev. Astron. Astrophys.* **61**, 65–130 (2023).
3. Bromm, V. & Loeb, A. The formation of the first low-mass stars from gas with low carbon and oxygen abundances. *Nature* **425**, 812–814 (2003).
4. Schneider, R., Ferrara, A., Salvaterra, R., Omukai, K. & Bromm, V. Low-mass relics of early star formation. *Nature* **422**, 869–871 (2003).

5. Frebel, A. & Norris, J. E. Near-field cosmology with extremely metal-poor stars. *Annu. Rev. Astron. Astrophys.* **53**, 631–688 (2015).
6. Caffau, E. et al. An extremely primitive star in the Galactic halo. *Nature* **477**, 67–69 (2011).
7. Caffau, E. et al. SDSS J102915.14+172927.9: revisiting the chemical pattern. *Astron. Astrophys.* **691**, A245 (2024).
8. Christlieb, N. et al. A stellar relic from the early Milky Way. *Nature* **419**, 904–906 (2002).
9. Frebel, A. et al. Nucleosynthetic signatures of the first stars. *Nature* **434**, 871–873 (2005).
10. Keller, S. C. et al. A single low-energy, iron-poor supernova as the source of metals in the star SMSS J031300.36–670839.3. *Nature* **506**, 463–466 (2014).
11. Starkenburg, E. et al. The Pristine survey IV: approaching the Galactic metallicity floor with the discovery of an ultra-metal-poor star. *Mon. Not. R. Astron. Soc.* **481**, 3838–3852 (2018).
12. Limberg, G. et al. Discovery of an [Fe/H] ~ 4.8 star in Gaia XP spectra. *Astrophys. J. Lett.* **989**, L18 (2025).
13. Kollmeier, J. A. et al. Sloan Digital Sky Survey. V. Pioneering panoptic spectroscopy. *Astron. J.* **171**, 52 (2026).
14. Cargile, P. A. et al. MINESweeper: spectrophotometric modeling of stars in the Gaia era. *Astrophys. J.* **900**, 28 (2020).
15. Chandra, V. et al. Mapping the distant and metal-poor Milky Way with SDSS-V. Preprint at https://arxiv.org/abs/2508.00978 (2025).
16. Bernstein, R., Shectman, S. A., Gunnels, S. M., Mochnacki, S. & Athey, A. E. MIKE: a double echelle spectrograph for the Magellan telescopes at Las Campanas Observatory. *Proc. SPIE* **4841**, 1694–1704 (2003).
17. Gerber, J. M. et al. Non-LTE radiative transfer with Turbospectrum. *Astron. Astrophys.* **669**, A43 (2023).
18. Eitner, P. et al. M3DIS—a grid of 3D radiation-hydrodynamics stellar atmosphere models for stellar surveys. I. Procedure, validation, and the Sun. *Astron. Astrophys.* **688**, A52 (2024).
19. Placco, V. M., Frebel, A., Beers, T. C. & Stancliffe, R. J. Carbon-enhanced metal-poor star frequencies in the Galaxy: corrections for the effect of evolutionary status on carbon abundances. *Astrophys. J.* **797**, 21 (2014).
20. Lind, K., Primas, F., Charbonnel, C., Grundahl, F. & Asplund, M. Signatures of intrinsic Li depletion and Li-Na anti-correlation in the metal-poor globular cluster NGC 6397. *Astron. Astrophys.* **503**, 545–557 (2009).
21. Cayrel, R. et al. First stars V—abundance patterns from C to Zn and supernova yields in the early Galaxy. *Astron. Astrophys.* **416**, 1117–1138 (2004).
22. Lai, D. K. et al. Detailed abundances for 28 metal-poor stars: stellar relics in the Milky Way. *Astrophys. J.* **681**, 1524–1556 (2008).
23. Howes, L. M. et al. Extremely metal-poor stars from the cosmic dawn in the bulge of the Milky Way. *Nature* **527**, 484–487 (2015).
24. Simon, J. D. et al. Chemical signatures of the first supernovae in the Sculptor dwarf spheroidal galaxy. *Astrophys. J.* **802**, 93 (2015).
25. Skúladóttir, Á, Vanni, I., Salvadori, S. & Lucchesi, R. Tracing population III supernovae with extreme energies through the Sculptor dwarf spheroidal galaxy. *Astron. Astrophys.* **681**, A44 (2024).
26. Chiti, A. et al. Enrichment by extragalactic first stars in the Large Magellanic Cloud. *Nat. Astron.* **8**, 637–647 (2024).
27. Lodders, K., Bergemann, M. & Palme, H. Solar System elemental abundances from the solar photosphere and CI-chondrites. *Space Sci. Rev.* **221**, 23 (2025).
28. Lagae, C. et al. Raising the observed metallicity floor with a 3D non-LTE analysis of SDSS J102915.14+172927.9. *Astron. Astrophys.* **672**, A90 (2023).
29. Nordlander, T. et al. 3D NLTE analysis of the most iron-deficient star, SMSS0313–6708. *Astron. Astrophys.* **597**, A6 (2017).
30. Sestito, F. et al. Tracing the formation of the Milky Way through ultra metal-poor stars. *Mon. Not. R. Astron. Soc.* **484**, 2166–2180 (2019).
31. Ji, A. P. et al. Detailed abundances in the ultra-faint Magellanic satellites Carina II and III. *Astrophys. J.* **889**, 27 (2020).
32. Chiti, A. et al. Enrichment by the first stars in a relic dwarf galaxy. *Nat. Astron.* https://doi.org/10.1038/s41550-026-02802-z (2026).
33. Schneider, R., Omukai, K., Bianchi, S. & Valiante, R. The first low-mass stars: critical metallicity or dust-to-gas ratio? *Mon. Not. R. Astron. Soc.* **419**, 1566–1575 (2012).
34. Frebel, A., Johnson, J. L. & Bromm, V. Probing the formation of the first low-mass stars with stellar archaeology. *Mon. Not. R. Astron. Soc.* **380**, L40–L44 (2007).
35. Schneider, R. et al. The formation of the extremely primitive star SDSS J102915+172927 relies on dust. *Mon. Not. R. Astron. Soc.* **423**, L60–L64 (2012).
36. Chiaki, G., Tominaga, N. & Nozawa, T. Classification of extremely metal-poor stars: absent region in A(C)–[Fe/H] plane and the role of dust cooling. *Mon. Not. R. Astron. Soc.* **472**, L115–L119 (2017).
37. Frebel, A., Johnson, J. L. & Bromm, V. The minimum stellar metallicity observable in the Galaxy. *Mon. Not. R. Astron. Soc.* **392**, L50–L54 (2009).
38. Shen, S., Kulkarni, G., Madau, P. & Mayer, L. Chemical enrichment of stars due to accretion from the ISM during the Galaxy's assembly. *Mon. Not. R. Astron. Soc.* **469**, 4012–4021 (2017).
39. Heger, A. & Woosley, S. E. Nucleosynthesis and evolution of massive metal-free stars. *Astrophys. J.* **724**, 341–373 (2010).
40. Johnson, J. L. & Bromm, V. The cooling of shock-compressed primordial gas. *Mon. Not. R. Astron. Soc.* **366**, 247–256 (2006).
41. McKee, C. F. & Tan, J. C. The formation of the first stars. II. Radiative feedback processes and implications for the initial mass function. *Astrophys. J.* **681**, 771–797 (2008).
42. Madau, P., Ferrara, A. & Rees, M. J. Early metal enrichment of the intergalactic medium by pregalactic outflows. *Astrophys. J.* **555**, 92–105 (2001).
43. Clark, P. C., Glover, S. C. O., Klessen, R. S. & Bromm, V. Gravitational fragmentation in turbulent primordial gas and the initial mass function of population III stars. *Astrophys. J.* **727**, 110 (2011).
44. Fujimoto, S. et al. GLIMPSE: an ultrafaint $\simeq 10^5 M_\odot$ Pop III galaxy candidate and first constraints on the Pop III UV luminosity function at $z \simeq 6$–7. *Astrophys. J.* **989**, 46 (2025).
45. Nakajima, K. et al. An ultra-faint, chemically primitive galaxy forming at the epoch of reionization. Preprint at https://arxiv.org/abs/2506.11846 (2025).
46. Morishita, T. et al. Pristine massive star formation caught at the break of cosmic dawn. Preprint at https://arxiv.org/abs/2507.10521 (2025).
47. Katz, H., Kimm, T., Ellis, R. S., Devriendt, J. & Slyz, A. The challenges of identifying population III stars in the early Universe. *Mon. Not. R. Astron. Soc.* **524**, 351–360 (2023).
48. Smee, S. A. et al. The multi-object, fiber-fed spectrographs for the Sloan Digital Sky Survey and the Baryon Oscillation Spectroscopic Survey. *Astron. J.* **146**, 32 (2013).
49. Schlaufman, K. C. & Casey, A. R. The best and brightest metal-poor stars. *Astrophys. J.* **797**, 13 (2014).
50. Conroy, C. et al. They might be giants: an efficient color-based selection of red giant stars. *Astrophys. J.* **861**, L16 (2018).
51. Conroy, C. et al. All-sky dynamical response of the Galactic halo to the Large Magellanic Cloud. *Nature* **592**, 534–536 (2021).
52. Chandra, V., Naidu, R. P., Conroy, C. et al. Discovery of the Magellanic Stellar Stream out to 100 kpc. *Astrophys. J.* **956**, 110 (2023b).
53. Kelson, D. D. Optimal techniques in two-dimensional spectroscopy: background subtraction for the 21st century. *Publ. Astron. Soc. Pac.* **115**, 688–699 (2003).

54. Ji, A. P. et al. LESSPayne: labeling echelle spectra with SMHR and Payne. *Astrophysics Source Code Library* ascl:2503.025 (2025).
55. Ting, Y.-S., Conroy, C., Rix, H.-W. & Cargile, P. The Payne: self-consistent ab initio fitting of stellar spectra. *Astrophys. J.* **879**, 69 (2019).
56. Casey, A. R. *A Tale of Tidal Tales in the Milky Way*. PhD thesis, Australian National Univ., Canberra (2014).
57. Mucciarelli, A., Bellazzini, M. & Massari, D. Exploiting the Gaia EDR3 photometry to derive stellar temperatures. *Astron. Astrophys.* **653**, A90 (2021).
58. Schlafly, E. F. & Finkbeiner, D. P. Measuring reddening with Sloan Digital Sky Survey Stellar spectra and recalibrating SFD. *Astrophys. J.* **737**, 103 (2011).
59. Schlegel, D. J., Finkbeiner, D. P. & Davis, M. Maps of dust infrared emission for use in estimation of reddening and cosmic microwave background radiation foregrounds. *Astrophys. J.* **500**, 525–553 (1998).
60. Morton, T. D. isochrones: stellar model grid package. *Astrophysics Source Code Library* ascl:1503.010 (2015).
61. Feroz, F. & Hobson, M. P. Multimodal nested sampling: an efficient and robust alternative to Markov chain Monte Carlo methods for astronomical data analyses. *Mon. Not. R. Astron. Soc.* **384**, 449–463 (2008).
62. Choi, J. et al. Mesa Isochrones and Stellar Tracks (MIST). I. Solar-scaled models. *Astrophys. J.* **823**, 102 (2016).
63. Gaia Collaboration et al. Gaia Early Data Release 3. Summary of the contents and survey properties. *Astron. Astrophys.* **649**, A1 (2021).
64. Fabricius, C. et al. Gaia Early Data Release 3. Catalogue validation. *Astron. Astrophys.* **649**, A5 (2021).
65. Lindegren, L. et al. Gaia Early Data Release 3. Parallax bias versus magnitude, colour, and position. *Astron. Astrophys.* **649**, A4 (2021).
66. Lindegren, L. et al. Gaia Early Data Release 3. The astrometric solution. *Astron. Astrophys.* **649**, A2 (2021).
67. Rowell, N. et al. Gaia Early Data Release 3. Modelling and calibration of Gaia's point and line spread functions. *Astron. Astrophys.* **649**, A11 (2021).
68. Torra, F. et al. Gaia Early Data Release 3. Building the Gaia DR3 source list—cross-match of Gaia observations. *Astron. Astrophys.* **649**, A10 (2021).
69. Bianchi, L., Shiao, B. & Thilker, D. Revised catalog of GALEX ultraviolet sources. I. The All-Sky Survey: GUVcat_AIS. *Astrophys. J. Suppl. Ser.* **230**, 24 (2017).
70. Onken, C. A. et al. SkyMapper Southern Survey: Data Release 4. *Publ. Astron. Soc. Aust.* **41**, e061 (2024).
71. Gaia Collaboration et al. The Gaia mission. *Astron. Astrophys.* **595**, A1 (2016).
72. Riello, M. et al. Gaia Early Data Release 3. Photometric content and validation. *Astron. Astrophys.* **649**, A3 (2021).
73. Skrutskie, M. F. et al. The Two Micron All Sky Survey (2MASS). *Astron. J.* **131**, 1163–1183 (2006).
74. Wright, E. L. et al. The Wide-field Infrared Survey Explorer (WISE): mission description and initial on-orbit performance. *Astron. J.* **140**, 1868–1881 (2010).
75. Mainzer, A. et al. Preliminary results from NEOWISE: an enhancement to the Wide-field Infrared Survey Explorer for Solar System science. *Astrophys. J.* **731**, 53 (2011).
76. Eisenhardt, P. R. M. et al. The CatWISE preliminary catalog: motions from WISE and NEOWISE data. *Astrophys. J. Suppl. Ser.* **247**, 69 (2020).
77. Marocco, F. et al. The CatWISE2020 Catalog. *Astrophys. J. Suppl. Ser.* **253**, 8 (2021).
78. Bailer-Jones, C. A. L., Rybizki, J., Fouesneau, M., Demleitner, M. & Andrae, R. Estimating distances from parallaxes. V. Geometric and photogeometric distances to 1.47 billion stars in Gaia Early Data Release 3. *Astron. J.* **161**, 147 (2021).
79. Husser, T. O. et al. A new extensive library of PHOENIX stellar atmospheres and synthetic spectra. *Astron. Astrophys.* **553**, A6 (2013).
80. Stassun, K. G., Collins, K. A. & Gaudi, B. S. Accurate empirical radii and masses of planets and their host stars with Gaia parallaxes. *Astron. J.* **153**, 136 (2017).
81. Stassun, K. G., Corsaro, E., Pepper, J. A. & Gaudi, B. S. Empirical accurate masses and radii of single stars with TESS and Gaia. *Astron. J.* **155**, 22 (2018).
82. Frebel, A., Casey, A. R., Jacobson, H. R. & Yu, Q. Deriving stellar effective temperatures of metal-poor stars with the excitation potential method. *Astrophys. J.* **769**, 57 (2013).
83. Sneden, C. A. *Carbon and Nitrogen Abundances in Metal-Poor Stars*. PhD thesis, Univ. Texas, Austin (1973).
84. Sobeck, J. S. et al. The abundances of neutron-capture species in the very metal-poor globular cluster M15: a uniform analysis of red giant branch and red horizontal branch stars. *Astron. J.* **141**, 175 (2011).
85. Sneden, C., Bean, J., Ivans, I., Lucatello, S. & Sobeck, J. MOOG: LTE line analysis and spectrum synthesis. *Astrophysics Source Code Library* ascl:1202.009 (2012).
86. Kurucz, R. L. Model atmospheres for G, F, A, B, and O stars. *Astrophys. J. Suppl. Ser.* **40**, 1–340 (1979).
87. Castelli, F. & Kurucz, R. L. New grids of ATLAS9 model atmospheres. *IAU Symp.* **210**, A20 (2003).
88. Plez, B. Turbospectrum: code for spectral synthesis. *Astrophysics Source Code Library* ascl:1205.004 (2012).
89. Gustafsson, B. et al. A grid of MARCS model atmospheres for late-type stars. I. Methods and general properties. *Astron. Astrophys.* **486**, 951–970 (2008).
90. Bergemann, M., Lind, K., Collet, R., Magic, Z. & Asplund, M. Non-LTE line formation of Fe in late-type stars—I. Standard stars with 1D and <3D> model atmospheres. *Mon. Not. R. Astron. Soc.* **427**, 27–49 (2012).
91. Carlsson, M. *A Computer Program for Solving Multi-level Non-LTE Radiative Transfer Problems in Moving Or Static Atmospheres* Uppsala Astronomical Observatory Reports (1986).
92. Wheeler, A. J., Abruzzo, M. W., Casey, A. R. & Ness, M. K. KORG: a modern 1D LTE spectral synthesis package. *Astron. J.* **165**, 68 (2023).
93. Wheeler, A. J., Casey, A. R. & Abruzzo, M. W. Korg: fitting, model atmosphere interpolation, and Brackett lines. *Astron. J.* **167**, 83 (2024).
94. Casey, A. R. & Schlaufman, K. C. The universality of the rapid neutron-capture process revealed by a possible disrupted dwarf galaxy star. *Astrophys. J.* **850**, 179 (2017).
95. Ricker, G. R. et al. Transiting Exoplanet Survey Satellite (TESS). *J. Astron. Telesc. Instrum. Syst.* **1**, 014003 (2015).
96. Stello, D. et al. TESS asteroseismology of the Kepler red giants. *Mon. Not. R. Astron. Soc.* **512**, 1677–1686 (2022).
97. Brasseur, C. E., Phillip, C., Fleming, S. W., Mullally, S. E. & White, R. L. Astrocut: Tools for creating cutouts of TESS images. *Astrophysics Source Code Library* ascl:1905.007 (2019).
98. Lightkurve Collaboration et al. Lightkurve: Kepler and TESS time series analysis in Python. *Astrophysics Source Code Library* ascl:1812.013 (2018).
99. Lomb, N. R. Least-squares frequency analysis of unequally spaced data. *Astrophys. Space Sci.* **39**, 447–462 (1976).
100. Scargle, J. D. Studies in astronomical time series analysis. II. Statistical aspects of spectral analysis of unevenly spaced data. *Astrophys. J.* **263**, 835–853 (1982).
101. Howell, M., Campbell, S. W., Kalup, C., Stello, D. & De Silva, G. M. Asteroseismic masses of red giants in the galactic globular clusters M9 and M19. *Mon. Not. R. Astron. Soc.* **536**, 1389–1407 (2025).

102. Kjeldsen, H. & Bedding, T. R. Amplitudes of stellar oscillations: the implications for asteroseismology. *Astron. Astrophys.* **293**, 87–106 (1995).
103. Epstein, C. R. et al. Testing the asteroseismic mass scale using metal-poor stars characterized with APOGEE and Kepler. *Astrophys. J. Lett.* **785**, L28 (2014).
104. Schonhut-Stasik, J. et al. The APO-K2 catalog. I. 7500 red giants with fundamental stellar parameters from APOGEE DR17 spectroscopy and K2-GAP asteroseismology. *Astron. J.* **167**, 50 (2024).
105. Huber, D. et al. Stellar models are reliable at low metallicity: an asteroseismic age for the ancient very metal-poor star KIC 8144907. *Astrophys. J.* **975**, 19 (2024).
106. Larsen, J. R. et al. Pushing the boundaries of asteroseismic individual frequency modelling: unveiling two evolved very low-metallicity red giants. *Astron. Astrophys.* **697**, A153 (2025).
107. Ji, A. P. et al. Metal mixing in the r-process enhanced ultrafaint dwarf galaxy reticulum II. *Astron. J.* **165**, 100 (2023).
108. Karovicova, I. et al. Fundamental stellar parameters of benchmark stars from CHARA interferometry. I. Metal-poor stars. *Astron. Astrophys.* **640**, A25 (2020).
109. Martin, N. F. et al. A stellar stream remnant of a globular cluster below the metallicity floor. *Nature* **601**, 45–48 (2022).
110. Caffau, E. et al. Unveiling the nature of HE 0107−5240: a long period binary CEMP-no star with [Fe/H] of −5.56. *Astron. Astrophys.* **704**, A238 (2025).
111. Bergemann, M. et al. Non-local thermodynamic equilibrium stellar spectroscopy with 1D and <3D> models. I. Methods and application to magnesium abundances in standard stars. *Astrophys. J.* **847**, 15 (2017).
112. Lind, K., Bergemann, M. & Asplund, M. Non-LTE line formation of Fe in late-type stars—II. 1D spectroscopic stellar parameters. *Mon. Not. R. Astron. Soc.* **427**, 50–60 (2012).
113. Mashonkina, L., Sitnova, T. & Belyaev, A. K. Influence of inelastic collisions with hydrogen atoms on the non-LTE modelling of Ca I and Ca II lines in late-type stars. *Astron. Astrophys.* **605**, A53 (2017).
114. Ezzeddine, R. et al. An empirical recipe for inelastic hydrogen-atom collisions in non-LTE calculations. *Astron. Astrophys.* **618**, A141 (2018).
115. Tayar, J. et al. The correlation between mixing length and metallicity on the giant branch: implications for ages in the Gaia era. *Astrophys. J.* **840**, 17 (2017).
116. Choi, J., Dotter, A., Conroy, C. & Ting, Y.-S. On the red giant branch: ambiguity in the surface boundary condition leads to ≈100 K uncertainty in model effective temperatures. *Astrophys. J.* **860**, 131 (2018).
117. Casagrande, L. & VandenBerg, D. A. On the use of Gaia magnitudes and new tables of bolometric corrections. *Mon. Not. R. Astron. Soc.* **479**, L102–L107 (2018).
118. Ji, A. P. et al. The Southern Stellar Stream Spectroscopic Survey (S^5): chemical abundances of seven stellar streams. *Astron. J.* **160**, 181 (2020).
119. Placco, V. M. et al. Linemake: an atomic and molecular line list generator. *Res. Notes Am. Astron. Soc.* **5**, 92 (2021).
120. Heiter, U. et al. Atomic data for the Gaia-ESO Survey. *Astron. Astrophys.* **645**, A106 (2021).
121. Kupka, F., Piskunov, N., Ryabchikova, T. A., Stempels, H. C. & Weiss, W. W. VALD-2: progress of the Vienna Atomic Line Data Base. *Astron. Astrophys. Suppl.* **138**, 119–133 (1999).
122. Bergemann, M. et al. Red supergiant stars as cosmic abundance probes. II. NLTE effects in J-band silicon lines. *Astrophys. J.* **764**, 115 (2013).
123. Magg, E. et al. Observational constraints on the origin of the elements. IV. Standard composition of the Sun. *Astron. Astrophys.* **661**, A140 (2022).
124. Semenova, E. et al. The Gaia-ESO survey: 3D NLTE abundances in the open cluster NGC 2420 suggest atomic diffusion and turbulent mixing are at the origin of chemical abundance variations. *Astron. Astrophys.* **643**, A164 (2020).
125. Bergemann, M. Ionization balance of Ti in the photospheres of the Sun and four late-type stars. *Mon. Not. R. Astron. Soc.* **413**, 2184–2198 (2011).
126. Bergemann, M. & Cescutti, G. Chromium: NLTE abundances in metal-poor stars and nucleosynthesis in the Galaxy. *Astron. Astrophys.* **522**, A9 (2010).
127. Bergemann, M. et al. Observational constraints on the origin of the elements. I. 3D NLTE formation of Mn lines in late-type stars. *Astron. Astrophys.* **631**, A80 (2019).
128. Bergemann, M., Pickering, J. C. & Gehren, T. NLTE analysis of CoI/CoII lines in spectra of cool stars with new laboratory hyperfine splitting constants. *Mon. Not. R. Astron. Soc.* **401**, 1334–1346 (2010).
129. Yakovleva, S. A., Belyaev, A. K. & Bergemann, M. Cobalt-hydrogen atomic and ionic collisional data. *Atoms* **8**, 34 (2020).
130. Bergemann, M. et al. Solar oxygen abundance. *Mon. Not. R. Astron. Soc.* **508**, 2236–2253 (2021).
131. Voronov, Y. V., Yakovleva, S. A. & Belyaev, A. K. Inelastic processes in nickel-hydrogen collisions. *Astrophys. J.* **926**, 173 (2022).
132. Lampton, M., Margon, B. & Bowyer, S. Parameter estimation in X-ray astronomy. *Astrophys. J.* **208**, 177–190 (1976).
133. Feldman, G. J. & Cousins, R. D. Unified approach to the classical statistical analysis of small signals. *Phys. Rev. D* **57**, 3873–3889 (1998).
134. Wilks, S. S. The large-sample distribution of the likelihood ratio for testing composite hypotheses. *Ann. Math. Stat.* **9**, 60 – 62 (1938).
135. Eitner, P. et al. M3DIS—a grid of 3D radiation-hydrodynamics stellar atmosphere models for stellar surveys: II. Carbon-enhanced metal-poor stars. *Astron. Astrophys.* **703**, A199 (2025).
136. Leenaarts, J. & Carlsson, M. in *The Second Hinode Science Meeting: Beyond Discovery-Toward Understanding*, *Astronomical Society of the Pacific Conference Series* Vol. 415 (eds Lites, B. et al.) 87–90 (Astronomical Society of the Pacific, 2009).
137. Masseron, T. et al. CH in stellar atmospheres: an extensive linelist. *Astron. Astrophys.* **571**, A47 (2014).
138. Akaike, H. Canonical correlation analysis of time series and the use of an information criterion. *Math. Sci. Eng.* **126**, 27–96 (1976).
139. Asplund, M., Nordlund, A. A., Trampedach, R. & Stein, R. F. 3D hydrodynamical model atmospheres of metal-poor stars. Evidence for a low primordial Li abundance. *Astron. Astrophys.* **346**, L17–L20 (1999).
140. Gratton, R. G., Sneden, C., Carretta, E. & Bragaglia, A. Mixing along the red giant branch in metal-poor field stars. *Astron. Astrophys.* **354**, 169–187 (2000).
141. Fraser, A. E., Joyce, M., Anders, E. H., Tayar, J. & Cantiello, M. Characterizing observed extra mixing trends in red giants using the reduced density ratio from thermohaline models. *Astrophys. J.* **941**, 164 (2022).
142. Tayar, J. & Joyce, M. Is thermohaline mixing the full story? Evidence for separate mixing events near the red giant branch bump. *Astrophys. J. Lett.* **935**, L30 (2022).
143. Reid, M. J. & Brunthaler, A. The proper motion of Sagittarius A*. II. The mass of Sagittarius A*. *Astrophys. J.* **616**, 872–884 (2004).
144. Drimmel, R. & Poggio, E. On the solar velocity. *Res. Notes Am. Astron. Soc.* **2**, 210 (2018).
145. GRAVITY Collaboration et al. A geometric distance measurement to the Galactic center black hole with 0.3% uncertainty. *Astron. Astrophys.* **625**, L10 (2019).
146. Price-Whelan, A. M. Gala: a Python package for galactic dynamics. *J. Open Source Softw.* **2**, 388 (2017).

147. Patel, E. et al. The orbital histories of Magellanic satellites using Gaia DR2 proper motions. *Astrophys. J.* **893**, 121 (2020).
148. Vasiliev, E. AGAMA: action-based galaxy modelling architecture. *Mon. Not. R. Astron. Soc.* **482**, 1525–1544 (2019).
149. Eilers, A.-C., Hogg, D. W., Rix, H.-W. & Ness, M. K. The circular velocity curve of the Milky Way from 5 to 25 kpc. *Astrophys. J.* **871**, 120 (2019).
150. Vasiliev, E., Belokurov, V. & Erkal, D. Tango for three: Sagittarius, LMC, and the Milky Way. *Mon. Not. R. Astron. Soc.* **501**, 2279–2304 (2021).
151. van der Marel, R. P., Alves, D. R., Hardy, E. & Suntzeff, N. B. New understanding of Large Magellanic Cloud structure, dynamics, and orbit from carbon star kinematics. *Astron. J.* **124**, 2639–2663 (2002).
152. Pietrzyński, G. et al. A distance to the Large Magellanic Cloud that is precise to one per cent. *Nature* **567**, 200–203 (2019).
153. Luri, X. et al. *Gaia EDR3 Documentation* Ch. 8 (European Space Agency, Gaia Data Processing and Analysis Consortium, 2021).
154. Yao, Y., Ji, A. P., Koposov, S. E. & Limberg, G. 200 000 candidate very metal-poor stars in Gaia DR3 XP spectra. *Mon. Not. R. Astron. Soc.* **527**, 10937–10954 (2024).
155. Yi, S. et al. Toward better age estimates for stellar populations: the Y^2 isochrones for solar mixture. *Astrophys. J. Suppl. Ser.* **136**, 417–437 (2001).
156. Demarque, P., Woo, J.-H., Kim, Y.-C. & Yi, S. K. Y^2 isochrones with an improved core overshoot treatment. *Astrophys. J. Suppl. Ser.* **155**, 667–674 (2004).
157. Collet, R., Asplund, M. & Trampedach, R. The chemical compositions of the extreme halo stars HE 0107–5240 and HE 1327–2326 inferred from three-dimensional hydrodynamical model atmospheres. *Astrophys. J. Lett.* **644**, L121–L124 (2006).
158. Norris, J. E. et al. HE 0557–4840: ultra-metal-poor and carbon-rich. *Astrophys. J.* **670**, 774–788 (2007).
159. Frebel, A., Collet, R., Eriksson, K., Christlieb, N. & Aoki, W. HE 1327–2326, an unevolved star with [Fe/H] < −5.0. II. New 3D–1D corrected abundances from a Very Large Telescope UVES spectrum. *Astrophys. J.* **684**, 588–602 (2008).
160. Cohen, J. G. et al. New extremely metal-poor stars in the Galactic Halo. *Astrophys. J.* **672**, 320–341 (2008).
161. Yong, D. et al. The most metal-poor stars. II. Chemical abundances of 190 metal-poor stars including 10 new stars with [Fe/H] ≤ −3.5. *Astrophys. J.* **762**, 26 (2013).
162. Roederer, I. U. et al. A search for stars of very low metal abundance. VI. Detailed abundances of 313 metal-poor stars. *Astron. J.* **147**, 136 (2014).
163. Hansen, T. et al. An elemental assay of very, extremely, and ultra-metal-poor stars. *Astrophys. J.* **807**, 173 (2015).
164. Placco, V. M. et al. Metal-poor stars observed with the Magellan Telescope. III. New extremely and ultra metal-poor stars from SDSS/SEGUE and insights on the formation of ultra metal-poor stars. *Astrophys. J.* **809**, 136 (2015).
165. Bonifacio, P. et al. TOPoS. II. On the bimodality of carbon abundance in CEMP stars. Implications on the early chemical evolution of galaxies. *Astron. Astrophys.* **579**, A28 (2015).
166. Li, H. et al. High-resolution spectroscopic studies of ultra metal-poor stars found in the LAMOST survey. *Publ. Astron. Soc. Jpn* **67**, 84 (2015).
167. Meléndez, J. et al. 2MASS J18082002–5104378: the brightest (V = 11.9) ultra metal-poor star. *Astron. Astrophys.* **585**, L5 (2016).
168. Placco, V. M. et al. Observational constraints on first-star nucleosynthesis. II. Spectroscopy of an ultra metal-poor CEMP-no star. *Astrophys. J.* **833**, 21 (2016).
169. Caffau, E. et al. TOPoS. III. An ultra iron-poor multiple CEMP system. *Astron. Astrophys.* **595**, L6 (2016).
170. Bonifacio, P. et al. TOPoS. IV. Chemical abundances from high-resolution observations of seven extremely metal-poor stars. *Astron. Astrophys.* **612**, A65 (2018).
171. Aguado, D. S., González Hernández, J. I., Allende Prieto, C. & Rebolo, R. Back to the lithium plateau with the [Fe/H] < −6 star J0023+0307. *Astrophys. J. Lett.* **874**, L21 (2019).
172. Frebel, A. et al. Chemical abundance signature of J0023+0307: a second-generation main-sequence star with [Fe/H] < −6. *Astrophys. J.* **871**, 146 (2019).
173. Nordlander, T. et al. The lowest detected stellar Fe abundance: the halo star SMSS J160540.18–144323.1. *Mon. Not. R. Astron. Soc.* **488**, L109–L113 (2019).
174. González Hernández, J. I., Aguado, D. S., Allende Prieto, C., Burgasser, A. J. & Rebolo, R. The extreme CNO-enhanced composition of the primitive iron-poor dwarf star J0815+4729. *Astrophys. J. Lett.* **889**, L13 (2020).
175. Placco, V. M. et al. BD+44°493: chemo-dynamical analysis and constraints on companion planetary masses from WIYN/NEID spectroscopy. *Astrophys. J.* **977**, 12 (2024).
176. Abohalima, A. & Frebel, A. JINAbase—a database for chemical abundances of metal-poor stars. *Astrophys. J. Suppl. Ser.* **238**, 36 (2018).
177. Suda, T. et al. Stellar Abundances for the Galactic Archeology (SAGA) Database—compilation of the characteristics of known extremely metal-poor stars. *Publ. Astron. Soc. Jpn* **60**, 1159 (2008).
178. Aguado, D. S., Allende Prieto, C., González Hernández, J. I., Rebolo, R. & Caffau, E. New ultra metal-poor stars from SDSS: follow-up GTC medium-resolution spectroscopy. *Astron. Astrophys.* **604**, A9 (2017).
179. Allende Prieto, C. et al. GTC follow-up observations of very metal-poor star candidates from DESI. *Astrophys. J.* **957**, 76 (2023).
180. Caffau, E. et al. A primordial star in the heart of the Lion. *Astron. Astrophys.* **542**, A51 (2012).
181. Bessell, M. S. & Norris, J. The ultra-metal-deficient (population III) red giant CD–38 245?. *Astrophys. J.* **285**, 622–636 (1984).
182. Mittal, S. & Roederer, I. U. New stellar parameters, metallicities, and elemental abundance ratios for 311 metal-poor stars. *Astron. J.* **169**, 172 (2025).
183. Skúladóttir, Á et al. Zero-metallicity hypernova uncovered by an ultra-metal-poor star in the Sculptor dwarf spheroidal galaxy. *Astrophys. J. Lett.* **915**, L30 (2021).
184. Lardo, C. et al. The Pristine survey—XIV. Chemical analysis of two ultra-metal-poor stars. *Mon. Not. R. Astron. Soc.* **508**, 3068–3083 (2021).
185. Bessell, M. S. et al. Nucleosynthesis in a primordial supernova: carbon and oxygen abundances in SMSS J031300.36–670839.3. *Astrophys. J. Lett.* **806**, L16 (2015).
186. Jeena, S. K., Banerjee, P. & Heger, A. On the core-collapse supernova explanation for LAMOST J1010+2358. *Mon. Not. R. Astron. Soc.* **527**, 4790–4796 (2024).
187. Mardini, M. K. et al. The Atari Disk, a metal-poor stellar population in the disk system of the Milky Way. *Astrophys. J.* **936**, 78 (2022).
188. Peimbert, M., Luridiana, V. & Peimbert, A. Revised primordial helium abundance based on new atomic data. *Astrophys. J.* **666**, 636–646 (2007).
189. Amarsi, A. M., Nissen, P. E. & Skúladóttir, Á. Carbon, oxygen, and iron abundances in disk and halo stars. Implications of 3D non-LTE spectral line formation. *Astron. Astrophys.* **630**, A104 (2019).
190. Asplund, M., Amarsi, A. M. & Grevesse, N. The chemical make-up of the Sun: a 2020 vision. *Astron. Astrophys.* **653**, A141 (2021).
191. Ji, A. P. et al. Spectacular nucleosynthesis from early massive stars. *Astrophys. J. Lett.* **961**, L41 (2024).

192. Smith, B. D. et al. Why does the Milky Way have a metallicity floor? *Mon. Not. R. Astron. Soc.* **532**, 3797–3807 (2024).
193. Bianchi, S. & Schneider, R. Dust formation and survival in supernova ejecta. *Mon. Not. R. Astron. Soc.* **378**, 973–982 (2007).
194. Ji, A. P., Frebel, A. & Bromm, V. The chemical imprint of silicate dust on the most metal-poor stars. *Astrophys. J.* **782**, 95 (2014).
195. Chiaki, G. et al. Supernova dust formation and the grain growth in the early universe: the critical metallicity for low-mass star formation. *Mon. Not. R. Astron. Soc.* **446**, 2659–2672 (2015).
196. Nozawa, T. et al. Evolution of dust in primordial supernova remnants: can dust grains formed in the ejecta survive and be injected into the early interstellar medium? *Astrophys. J.* **666**, 955–966 (2007).
197. Chiaki, G. et al. Dust grain growth and the formation of the extremely primitive star SDSS J102915+172927. *Mon. Not. R. Astron. Soc.* **439**, 3121–3127 (2014).
198. Ji, A. P. Extra data for 'A nearly pristine star from the Large Magellanic Cloud'. *Zenodo* https://doi.org/10.5281/zenodo.18483957 (2026).
199. Bergemann, M., Lodders, K. & Palme, H. in *Encyclopedia of Astrophysics* Vol. 2 (ed. Mandel, I.) 387–418 (Springer, 2026).
200. Ochsenbein, F., Bauer, P. & Marcout, J. The VizieR database of astronomical catalogues. *Astron. Astrophys. Suppl.* **143**, 23–32 (2000).

Acknowledgements

We acknowledge The College at University of Chicago for their support of undergraduate research that led to the identification of this star and supporting its analysis. This paper includes data gathered with the 6.5 meter Magellan Telescopes located at Las Campanas Observatory, Chile. We thank the staff at Las Campanas Observatory for their support making the observations possible. A.P.J. thanks A. Drlica-Wagner, H. Katz, J. Greene and D. Souto for useful discussions; and I. Roederer, I. Thompson and S. Shectman for a comparison spectrum of CD−38 245. We acknowledge support from the National Science Foundation under awards AST-2206264 (A.P.J., S.M.-T., Z.Z. and P.N.T.), AST-2338645 (K.C.S.) and DGE2139841 (W.C.). A.P.J. acknowledges the Alfred P. Sloan Research Fellowship and the University of Chicago's Research Computing Center. M.B. is supported through the Lise Meitner grant from the Max Planck Society and through the European Research Council (ERC) under the European Unions Horizon 2020 research and innovation programme (grant agreement number 949173). M.H. and J.A.J. acknowledge support from NASA grant 80NSSC24K0637. C.F.P.L. acknowledges funding from the European Research Council (ERC) under the European Union's Horizon 2020 research and innovation programme (grant agreement number 852839) and the Agence Nationale de la Recherche (ANR project ANR-24-CPJ1-0160-01). W.C. acknowledges support from a Gruber Science Fellowship at Yale University. J.G.F.-T. acknowledges the support provided by ANID Fondecyt Regular No. 1260371, ANID Fondecyt Postdoc No. 3230001 (sponsoring researcher), the Joint Committee ESO-Government of Chile under the agreement 2023 ORP 062/2023 and the support of the Doctoral Program in Artificial Intelligence, DISC-UCN. This project has been supported by the LP2021-9 Lendület grant of the Hungarian Academy of Sciences. This work benefited from a workshop supported by the National Science Foundation under grant number OISE-1927130 (IReNA), the Kavli Institute for Cosmological Physics, and the University of Chicago Data Science Institute. Funding for the Sloan Digital Sky Survey V has been provided by the Alfred P. Sloan Foundation, the Heising-Simons Foundation, the National Science Foundation and the participating institutions. SDSS acknowledges support and resources from the Center for High-Performance Computing at the University of Utah. SDSS telescopes are located at Apache Point Observatory, funded by the Astrophysical Research Consortium and operated by New Mexico State University, and at Las Campanas Observatory, operated by the Carnegie Institution for Science. The SDSS website is www.sdss.org. SDSS is managed by the Astrophysical Research Consortium for the Participating Institutions of the SDSS Collaboration, including the Carnegie Institution for Science, Chilean National Time Allocation Committee (CNTAC) ratified researchers, Caltech, the Gotham Participation Group, Harvard University, Heidelberg University, The Flatiron Institute, The Johns Hopkins University, L'Ecole polytechnique fédérale de Lausanne (EPFL), Leibniz-Institut für Astrophysik Potsdam (AIP), Max-Planck-Institut für Astronomie (MPIA Heidelberg), Max-Planck-Institut für Extraterrestrische Physik (MPE), Nanjing University, National Astronomical Observatories of China (NAOC), New Mexico State University, The Ohio State University, Pennsylvania State University, Smithsonian Astrophysical Observatory, Space Telescope Science Institute (STScI), the Stellar Astrophysics Participation Group, Universidad Nacional Autónoma de México, University of Arizona, University of Colorado Boulder, University of Illinois at Urbana-Champaign, University of Toronto, University of Utah, University of Virginia, Yale University, and Yunnan University. This work has made use of data from the European Space Agency (ESA) mission Gaia (https://www.cosmos.esa.int/gaia), processed by the Gaia Data Processing and Analysis Consortium (DPAC; https://www.cosmos.esa.int/web/gaia/dpac/consortium). Funding for the DPAC has been provided by national institutions, in particular the institutions participating in the Gaia Multilateral Agreement. Figure 3 uses a Gaia image by the Gaia Data Processing and Analysis Consortium (DPAC); A. Moitinho/A. F. Silva/M. Barros/C. Barata, University of Lisbon, Portugal; H. Savietto, Fork Research, Portugal. This paper includes data collected by the TESS mission. Funding for the TESS mission is provided by the NASA's Science Mission Directorate. The national facility capability for SkyMapper has been funded through ARC LIEF grant LE130100104 from the Australian Research Council, awarded to the University of Sydney, the Australian National University, Swinburne University of Technology, the University of Queensland, the University of Western Australia, the University of Melbourne, Curtin University of Technology, Monash University and the Australian Astronomical Observatory. SkyMapper is owned and operated by The Australian National University's Research School of Astronomy and Astrophysics. The survey data were processed and provided by the SkyMapper Team at ANU. The SkyMapper node of the All-Sky Virtual Observatory (ASVO) is hosted at the National Computational Infrastructure (NCI). Development and support of the SkyMapper node of the ASVO has been funded in part by Astronomy Australia Limited (AAL) and the Australian Government through the Commonwealth's Education Investment Fund (EIF) and National Collaborative Research Infrastructure Strategy (NCRIS), particularly the National eResearch Collaboration Tools and Resources (NeCTAR) and the Australian National Data Service Projects (ANDS). This publication makes use of data products from the Two Micron All-Sky Survey, which is a joint project of the University of Massachusetts and the Infrared Processing and Analysis Center/California Institute of Technology, funded by the National Aeronautics and Space Administration and the National Science Foundation. This publication makes use of data products from the Wide-field Infrared Survey Explorer, which is a joint project of the University of California, Los Angeles, and the Jet Propulsion Laboratory/California Institute of Technology, funded by the National Aeronautics and Space Administration. This research has made use of the VizieR catalogue access tool, CDS, Strasbourg, France. The original description of the VizieR service was published in ref. 200. This research has made use of NASA's Astrophysics Data System Bibliographic Services; the arXiv preprint server operated by Cornell University; and the SIMBAD databases hosted by the Strasbourg Astronomical Data Center.

Author contributions

A.P.J. led the conceptualization, MIKE observations, stellar parameter and chemical abundance analysis, population III analysis, writing, and interpretation. V.C. led the BOSS and kinematic analysis and contributed to writing and interpretation. S.M.-T. led the NLTE abundance analysis. Z.Z. led the literature compilation and total metallicity calculations, and contributed to the population III analysis and interpretation. S.M.-T. and Z.Z. contributed to the BOSS target selection. P.E. computed the 3D models and led the 3D LTE carbon analysis. K.C.S. led the distance determinations and contributed to stellar parameters, writing and interpretation. H.D.A., H.D., N.M.O., R.T. and P.N.T. contributed to the MIKE observations and the stellar parameter, chemical abundance, kinematic analysis and interpretation. K.G.S. contributed to the stellar parameter analysis, writing and interpretation. M.H. led the asteroseismology analysis. J.T. contributed to the carbon evolutionary corrections. M.B. contributed to the 3D and NLTE analyses. A.R.C. and J.A.J. contributed to the stellar parameter analysis. All authors contributed to the paper, interpretation, SDSS-V infrastructure and/or the SDSS-V high-resolution follow-up programme.

Competing interests

The authors declare no competing interests.

Additional information

Extended data is available for this paper at https://doi.org/10.1038/s41550-026-02816-7.

Supplementary information The online version contains supplementary material available at https://doi.org/10.1038/s41550-026-02816-7.

Correspondence and requests for materials should be addressed to Alexander P. Ji.

Peer review information *Nature Astronomy* thanks the anonymous reviewers for their contribution to the peer review of this work. Peer reviewer reports are available.

Reprints and permissions information is available at www.nature.com/reprints.

Publisher's note Springer Nature remains neutral with regard to jurisdictional claims in published maps and institutional affiliations.

[1]Department of Astronomy and Astrophysics, University of Chicago, Chicago, IL, USA. [2]Kavli Institute for Cosmological Physics, University of Chicago, Chicago, IL, USA. [3]NSF-Simons AI Institute for the Sky (SkAI), Chicago, IL, USA. [4]Center for Astrophysics | Harvard & Smithsonian, Cambridge, MA, USA. [5]Max Planck Institute for Astronomy, Heidelberg, Germany. [6]Heidelberg University, Heidelberg, Germany. [7]William H. Miller III Department of Physics and Astronomy, Johns Hopkins University, Baltimore, MD, USA. [8]Department of Physics and Astronomy, Vanderbilt University, Nashville, TN, USA. [9]Department of Astronomy and Center for Cosmology and AstroParticle Physics, The Ohio State University, Columbus, OH, USA. [10]Department of Astronomy, University of Florida, Gainesville, FL, USA. [11]School of Physics & Astronomy, Monash University, Clayton, Victoria, Australia. [12]Center for Computational Astrophysics, Flatiron Institute, New York, NY, USA. [13]Space Telescope Science Institute, Baltimore, MD, USA. [14]Department of Astronomy, Yale University, New Haven, CT, USA. [15]Núcleo UCN en Arqueología Galáctica - Inst. de Astronomía, Universidad Católica del Norte, Antofagasta, Chile. [16]Departamento de Ingeniería de Sistemas y Computación, Universidad Católica del Norte, Antofagasta, Chile. [17]Department of Astronomy, The University of Texas at Austin, Austin, TX, USA. [18]The Observatories of the Carnegie Institution for Science, Pasadena, CA, USA. [19]LIRA, Observatoire de Paris, Université PSL, Sorbonne Université, Université Paris Cité, CY Cergy Paris Université, CNRS, Meudon, France. [20]Institut de Ci'encies del Cosmos (ICCUB), Universitat de Barcelona, Barcelona, Spain. [21]Institut d'Estudis Espacials de Catalunya (IEEC), Barcelona, Spain. [22]Kavli IPMU (WPI), UTIAS, The University of Tokyo, Kashiwa, Chiba, Japan. [23]ELTE Eötvös Loránd University, Gothard Astrophysical Observatory, Szombathely, Hungary. [24]MTA-ELTE Lendület 'Momentum' Milky Way Research Group, Szombathely, Hungary. [25]HUN-REN CSFK, Konkoly Observatory; Eötvös Loránd University, Institute of Physics and Astronomy, Budapest, Hungary. [26]Department of Astronomy, University of Illinois at Urbana-Champaign, Urbana, IL, USA. [27]Department of Physics, Montana State University, Bozeman, MT, USA. [28]Center for Astrophysics and Space Astronomy, University of Colorado, Boulder, CO, USA. [29]Department of Astronomy & Astrophysics, The Pennsylvania State University, University Park, PA, USA. [30]The Institute for Gravitation for and the Cosmos, The Pennsylvania State University, University Park, PA, USA. ✉e-mail: alexji@uchicago.edu

https://doi.org/10.1038/s41550-026-02816-7

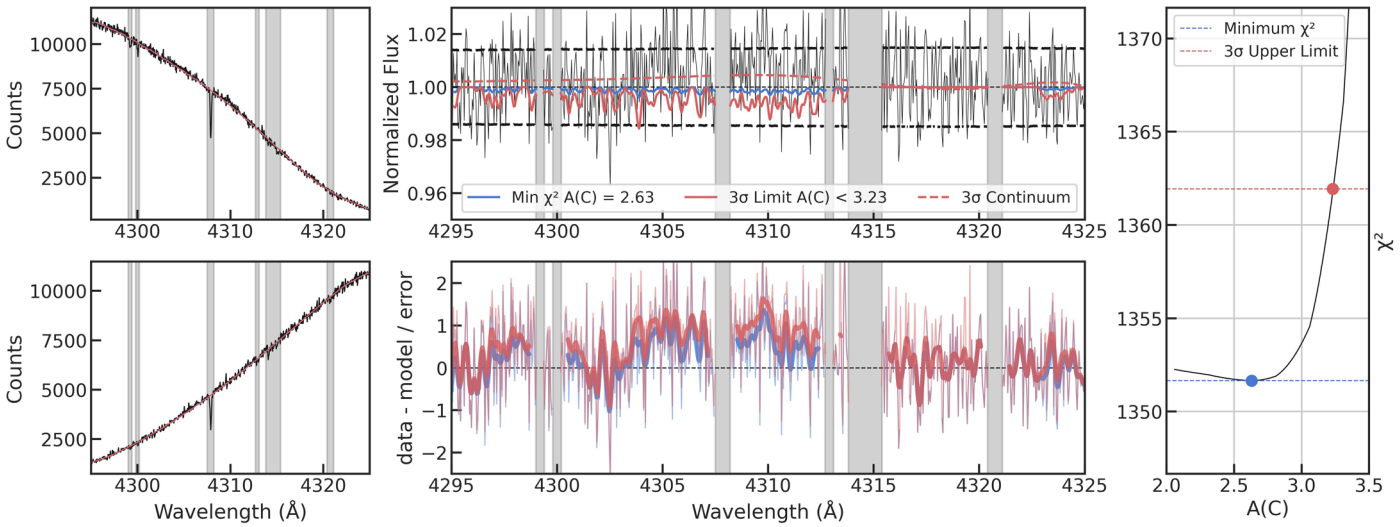

Extended Data Fig. 1 | Profile likelihood for CH upper limit. Left: the two spectral orders being fit with a 7th degree polynomial, the data is fit well. A red model is plotted indicating the 3σ upper limit, masked regions shown in grey. Center top: Stitched and normalized spectrum (black line, with 3σ pixel uncertainties shown as dashed black lines) compared to the best-fit (effectively no-carbon) spectrum (blue line) and the 3σ upper limit (red line). The data and blue lines are normalized to 1, while the red 3σ model is normalized to the dashed red 3σ continuum line. The dashed red line is not exactly at 1, because the continuum is redetermined at every value of A(C), resulting in a more conservative upper limit when compared to a fixed continuum by about 0.2 dex. We apply an extra +0.2 dex correction to the final results, as the 3D model's stellar parameters are not identical to our adopted parameters (see text). Center bottom: error-normalized residual for the best fit model (blue) and the 3σ upper limit (red). The per-pixel value is shown as a thin line, while the thick line is smoothed over 2 pixels. The red line is above the blue line where the CH features are. Note this is an approximation for visualization: the calculation is done on each order independently, not on the stitched spectrum. Right: χ^2 as a function of A(C). The blue point marks our minimum χ^2 value. The 3σ upper limit, corresponding to 99.9% confidence or $\Delta\chi^2 = 10.273$ for 1 degree of freedom, is marked as a red point.

https://doi.org/10.1038/s41550-026-02816-7

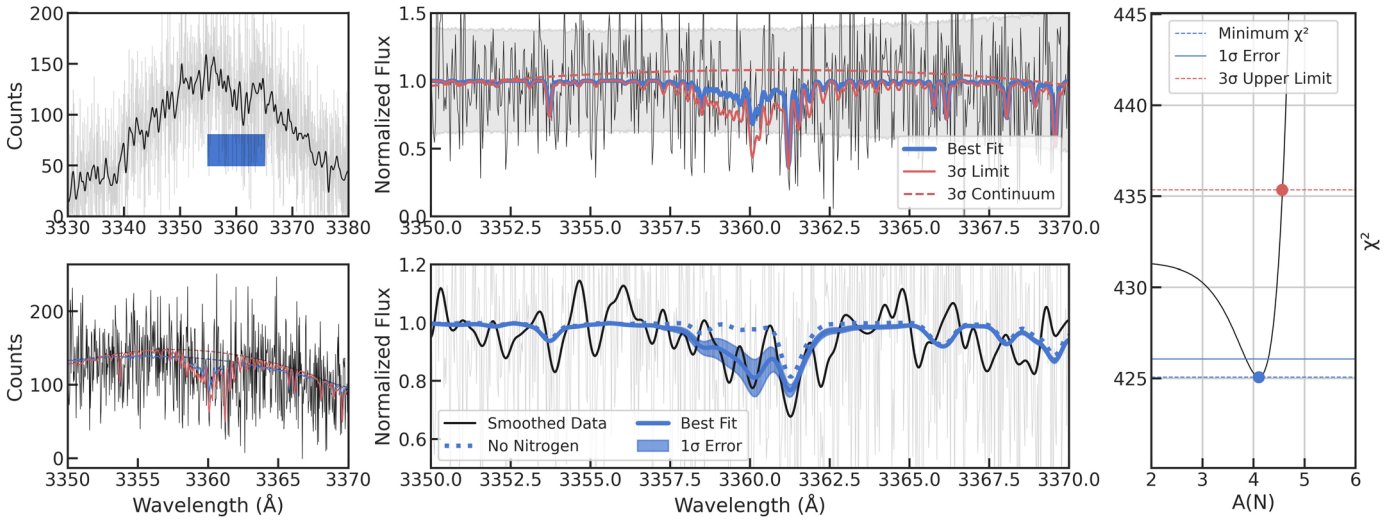

Extended Data Fig. 2 | Profile Likelihood for NH upper limit. Top Left: the full spectral order containing the NH band. The black line is smoothed by a Gaussian with 5 pixel FWHM, and the blue box indicates a wavelength region where there is a clear deviation from the echelle order shape. Bottom Left: the exact range being fit. The continuum (dashed lines) is modeled as a 2nd degree polynomial, which fits the data well. A blue model is plotted indicating the best fit, and a red model is plotted indicating the 3σ upper limit. Center top: Normalized spectrum (black line, with 1σ pixel uncertainties shown as black dashed lines) compared to the best-fit model (blue line) and the 3σ upper limit (red line). The data and blue lines are normalized to 1, while the red 3σ model is normalized to the dashed red 3σ continuum line. Center bottom: Smoothed visualization of the data. The best-fit model and 1σ uncertainties are shown in solid blue line/shaded region, while the model with no nitrogen is shown as a dotted blue line. Right: χ^2 as a function of A(N). The blue point marks the best-fit nitrogen value, A(N) = 4.10+0.18-0.25. The 3σ upper limit is A(N) <4.56 and marked as a red point.

https://doi.org/10.1038/s41550-026-02816-7

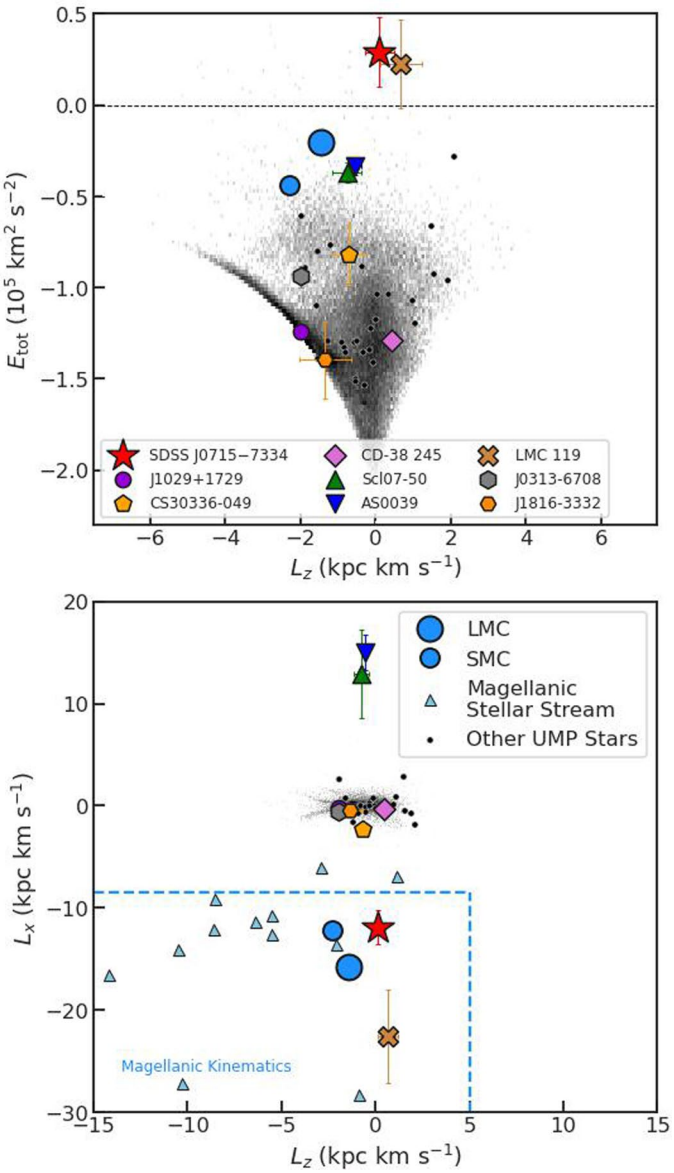

Extended Data Fig. 3 | Energy and angular momentum in a static potential. Top: Specific energy and angular momentum. J0715-7334 is shown as a large red star. Black points show a literature sample (see Literature Data Sample section in text). Large blue circles indicate the LMC and SMC. Colored points highlight eight notable metal-poor stars with 68% confidence uncertainties. The same stars are shown in the Main Text in Fig. 2. The shaded grey background is metal-poor stars from the SDSS-V halo program, computed in a static Milky Way gravitational potential (see Methods). J0715-7334 joins LMC-119[26] as originating from the LMC. Bottom: Galactocentric specific angular momentum in the Lz-Lx plane, in which stars associated with the Magellanic Clouds have a distinctive signature[52]. All halo stars from SDSS-V are shown, along with known ultra-metal-poor stars from the literature with 68% confidence uncertainties. Magellanic Stellar Stream members proposed by Chandra et al.[52] are shown, along with the selection box used to identify Magellanic Debris. J0715-7334 has kinematics that strongly associate it with the Clouds.

https://doi.org/10.1038/s41550-026-02816-7

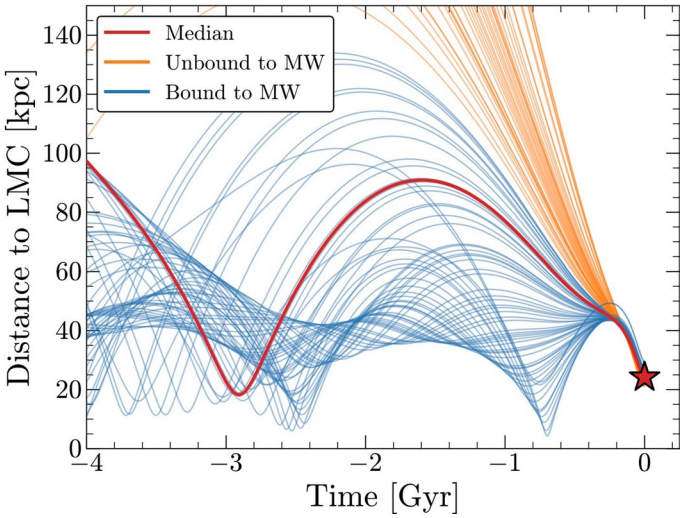

Extended Data Fig. 4 | Distance to LMC over time for different orbit integration samples. The thick red line shows the median orbit. The same orbit is shown in the Main Text in Fig. 3. The other lines are color-coded by the future fate of J0715-7334: orange lines show orbits that will be unbound to the Milky Way, while blue lines show orbits that will remain bound to the Milky Way.

https://doi.org/10.1038/s41550-026-02816-7

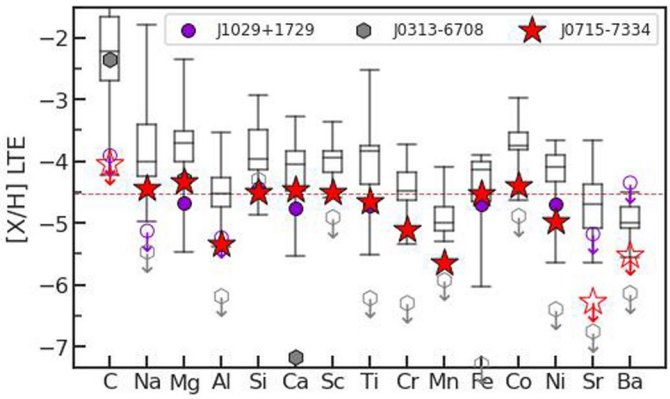

Extended Data Fig. 5 | 1D LTE abundances of SDSS J0715-7334 for different elements, compared to literature stars. Grey boxplots indicate the minimum, maximum, median, and 25-75 percentile [X/H] range for the literature stars in 1D LTE, where carbon has evolutionary corrections. Colored points highlight the 1D LTE analyses of SMSS J0313-6708[10] and J1029+1729[7]. A horizontal red line is drawn at the [Fe/H] value for J0715-7334.